Patricia Brunner

Design Optimization for Biomedical Soft Field Applications

Dissertation

Graz University of Technology

Institute for Medical Engineering
Head: Univ.-Prof. Dipl.-Ing. Dr. techn. Rudolf Stollberger

Supervisor: ao. Univ.-Prof. Dipl.-Ing. Dr. techn. Hermann Scharfetter

Graz, March 2016

Statutory Declaration

I declare that I have authored this thesis independently, that I have not used other than the declared sources/resources, and that I have explicitly marked all material which has been quoted either literally or by content from the used sources.

Graz, _____ _____

Date Signature

Eidesstattliche Erklärung[1]

Ich erkläre an Eides statt, dass ich die vorliegende Arbeit selbstständig verfasst, andere als die angegebenen Quellen/Hilfsmittel nicht benutzt, und die den benutzten Quellen wörtlich und inhaltlich entnommenen Stellen als solche kenntlich gemacht habe.

Graz, am _____ _____

Datum Unterschrift

[1] Beschluss der Curricula-Kommission für Bachelor-, Master- und Diplomstudien vom 10.11.2008; Genehmigung des Senates am 1.12.2008

For my loved ones.

Acknowledgments

The results of scientific work are never the achievements of one single person. On the contrary, they are only possible through a successful collaboration of many scientists.

Therefore, I want to thank everyone directly or indirectly involved in this work. First of all, I would like to thank my mentor Hermann Scharfetter for his motivation, scientific advice and guidance, and for introducing me into the interesting world of scientific research.

Without the preceding work of Christian Clason, the deterministic optimization of optode positions would not have been possible. His contributions were outstanding.

Many people from the Institute of Medical Engineering were really good friends – Robert Merwa, Michael Mayer, and Manuel Freiberger. Thank you for your moral support and many fruitful discussions.

For pointing out the difficulty of achieving a homogenous illumination for the photodynamic therapy of mesotheliomas in the thoracic cavity, I would like to thank Freya Smolle-Jüttner.

Last but not least, I would like to thank my whole family. For reminding me each and every day what really matters in life.

Abstract

Hard field applications are techniques (like X-ray and magnetic resonance imaging (MRI)) which utilize source signals that pass the medium in a predictable manner, independent of the material properties of the medium. Soft field applications such as bioimpedance analysis (BIA), optical tomography (OT), and electrical impedance tomography (EIT), on the other hand, are methods where the path of the source signals is determined by the electromagnetic properties of the medium.

Although soft field applications (SFAs) have the potential to be a useful non-invasive tool in clinical practice, they are not routinely used in hospitals yet. The two main problems of SFA are their low signal-to-noise ratio and their higher computational effort as compared to hard field applications.

This thesis presents two specific applications to illustrate approaches to overcome some of the specific problems in design optimization for SFA. Two articles in peer-reviewed journals provide the foundation for this work.

The first application deals with design optimization for BIA. It demonstrates how the estimation of body fats (BFs) and fat free mass (FFM) using impedance measurements can be improved. Using a realistic three-dimensional finite element (FE) model of the human thorax combined with a hierarchical model which directly incorporates all parameters of interest, a sensitivity analysis was carried out. The analysis revealed a high sensitivity to the subcutaneous fat layer thickness (SFL) and the fat content of the mesentery. The presented structural model is a prerequisite for a comprehensive investigation of body composition measurements and helps to gain further insight into BIA methods. Although this is a promising result, the intrinsic problem with BIA, namely the dependency of the results on the hydration state, still remains. Furthermore, the influence of changes in the

model geometry and the effect of models representing different values for the SFL has not been examined yet.

The second application shows the applicability of a novel mathematical method for the optimization of both the location as well as the strength of optical fibers for photodynamic therapy (PDT). This therapy combines light of a specific wavelength with a photosensitizer to chemically destroy tissue cells. Most commonly, it is employed for various oncological and dermatological treatments. PDT requires extremely homogeneous irradiation over the whole applicator to avoid ineffective treatment or even lethal overdoses. Simple two-dimensional as well as a realistic three-dimensional model of the human intrathoracic cavity were developed in this work. The coefficient of variation of the photon density on the surface of the applicator was used as an indicator for the homogeneity of illumination. The proposed method produces reasonable optode configurations resulting in homogeneous irradiation, although the number of required optodes is relatively high. Nevertheless, the algorithm is very efficient and does not need initial configuration. Using the same algorithm for other objectives is straightforward, and thus it could also be used for other design optimization problems without much additional effort.

Kurzfassung

Hartfeld-Anwendungen wie beispielsweise Röntgen und Magnetresonanztomographie (MRT) verwenden Quellsignale, welche ein Medium in vorhersehbarer Richtung durchqueren, unabhängig von dessen Materialeigenschaften. Im Gegensatz dazu verwenden Weichfeld-Anwendungen (wie zum Beispiel Bioimpedanzanalyse, optische Tomographie und elektrische Impedanztomographie) Quellsignale, deren Pfad durch ein Medium durch dessen elektromagnetische Eigenschaften bestimmt wird.

Obwohl Weichfeld-Anwendungen großes Potential als nicht-invasive Verfahren in der klinischen Praxis haben, werden sie heutzutage noch nicht routinemäßig in Krankenhäusern eingesetzt. Die zwei größten Probleme von Weichfeld- im Vergleich zu Hartfeld-Anwendungen sind deren geringes Signal-Rauschverhältnis sowie ein hoher Rechenaufwand.

Diese Arbeit stellt zwei spezifische Anwendungen vor, welche Möglichkeiten zur Lösung bestimmter Aspekte der genannten Probleme in der Design-Optimierung aufzeigen. Zwei in internationalen Fachzeitschriften veröffentlichte Artikel bilden die Grundlage für diese Arbeit.

Die erste Anwendung befasst sich mit der Design-Optimierung für die Bioimpedanzanalyse (BIA). Sie zeigt, wie die Schätzung der Körperfette sowie der fettfreien Masse mittels Impedanzmessungen verbessert werden kann. Mit einem realistischen dreidimensionalen Finiten Elemente (FE) Modell des menschlichen Thorax in Kombination mit einem hierarchischen Modell, welches alle zu schätzenden Parameter enthält, wurde eine Sensitivitätsanalyse durchgeführt. Diese Analyse ergab eine hohe Sensitivität sowohl für die subkutane Fettschicht als auch für das Fettgewebe des Mesenteriums. Das verwendete strukturelle Modell ist eine notwendige Voraussetzung für eine umfassende Analyse von Körperzusammensetzungsmessungen und ermöglicht weitergehende Einsichten in BIA-Methoden. Obwohl dies ein

vielversprechendes Ergebnis ist, bleibt das intrinsische Problem von BIA, nämlich die Abhängigkeit der Ergebnisse vom Hydrationszustand, weiter bestehen. Darüber hinaus wurde der Einfluss von Änderungen der Modellgeometrie und der Effekt von verschiedenen Modellen für unterschiedliche subkutane Fettschichtdicken noch nicht untersucht.

Die zweite Anwendung zeigt die Verwendung einer neuen mathematischen Methode für die Optimierung der Position und der Stärke der optischen Fasern in der photodynamischen Therapie (PDT). Diese Therapie kombiniert Licht einer spezifischen Wellenlänge mit einem Photosensitizer, um gezielt Zellgewebe chemisch zu zerstören. Häufig wird sie in der onkologischen und dermatologischen Behandlung eingesetzt. PDT benötigt eine extrem homogene Ausleuchtung über den gesamten Applikator um ineffiziente Behandlungen oder sogar tödliche Überdosierungen zu verhindern. Einfache zweidimensionale sowie ein realistisches dreidimensionales Modell der menschlichen Brusthöhle wurden im Rahmen dieser Arbeit entwickelt. Der Variationskoeffizient der Photonendichte auf der Oberfläche des Applikators wurde als Indikator für die Homogenität der Ausleuchtung verwendet. Die vorgestellte Methode erzeugt vernünftige Optodenkonfigurationen mit homogener Ausleuchtung, wobei die Anzahl der benötigten Optoden relativ hoch ist. Nichtsdestotrotz ist der verwendete Algorithmus sehr effizient und benötigt keine Initialisierung. Die Verwendung des Algorithmus für andere Methoden ist einfach möglich, und daher könnte er ohne größeren Aufwand für andere Design-Optimierungsaufgaben eingesetzt werden.

Contents

List of Figures

List of Tables

1 Introduction

Biomedical applications can be classified as soft field and hard field applications. On the one hand, techniques such as X-ray and magnetic resonance imaging (MRI) utilize source signal that pass through the medium in a predictable manner (independent of the material properties of the medium). These methods are referred to as hard field applications. On the other hand, methods where the path of the source signals is determined by the electrical properties of the medium are called soft field applications (see e. g. Mukhopadhyay, Lay-Ekuakille, and Fuchs, 2011). Soft field applications (SFAs) commonly use electromagnetic fields to estimate material properties of (biological) samples. Examples for these methods include electrical impedance tomography (EIT) (Bayford, 2006), bioimpedance analysis (BIA) (Kyle et al., 2004a), magnetic induction tomography (MIT) (Griffiths, 2001), optical tomography (OT) (Arridge, 1999), and near infrared spectroscopy (NIRS) (Ferrari and Quaresima, 2012).

For many years, research in the field of SFAs has focused on exploring new ways to develop reliable instruments for medical purposes. Although many problems are not easy to overcome, practical applications are emerging. SFAs have several compelling advantages: they are inexpensive, non-invasive, and they can be continuously applied in a straightforward way. In addition, they can be used 24 hours a day. Therefore, SFAs perfectly complement other methods like computer tomography (CT) or MRI.

The challenge in SFAs is to extract information about the investigated sample based on the measurement data. The inverse problem is, by definition, the inverse to the forward problem. Two problems are inverse to each other if the formulation of one problem involves all or part of the solution of the other one (Keller, 1976). The forward problem means the prediction of data using a physical or mathematical model which incorporates a

set of known model parameters (e. g. geometry information, conductivity distribution). Opposed to that, an inverse problem estimates an unknown set of model parameters using a physical or mathematical model with a set of data. An example of a well-studied inverse problem is the so-called Calderón problem for EIT. It addresses the question of determining the electrical conductivity distribution inside a body using voltage and current measurements on the body surface (Calderón, 2006). Further examples of inverse problems include the identification of physiological parameters (such as hydration) from measurements made on the body surface, the identification of boundary shapes and their interfaces with a region of interest, and the development of a mathematical model using observed (noisy) data.

The corresponding direct (forward) problems are usually well-posed with an existing, unique, and stable solution. In contrast, the solutions of the corresponding inverse problems are usually ill-posed (in the case of continuous systems) or ill-conditioned (in the case of discrete linear systems). In addition, electromagnetic field problems are often nonlinear.

Although SFA methods are not established in medical use yet, they have the potential to complement standard medical procedures, guide treatment, and improve treatment outcome. Some examples for promising applications are:

- Electromagnetic techniques like EIT, OT, microwave tomograhpy (MT), and especially a combination of these approaches, have the potential to improve early non-invasive breast cancer screening (Hassan and El-Shenawee, 2011; El-Shenawee, 2011). In standard preventive medical checkups, X-ray mammography is routinely used for breast cancer detection. However, this technique does not only have a low sensitivity (4 % to 34 % false negative results) (Huynh, Jarolimek, and Daye, 1998) as well as a low specificity (8 % to 21 % false positive results) (Hofvind et al., 2012), but the ionizing radiation in X-ray mammography means a higher risk for cancer. Alternative methods like MRI and ultrasound are either very expensive or have low sensitivities.
- EIT systems are already sufficiently developed to monitor lung ventilation (Adler et al., 2012). Consequently, EIT could be established as a reliable, reproducible, and relevant technique in clinics to improve

patient treatment, for example for infants with respiratory distress syndrome (Chatziioannidis et al., 2013).
- Several studies have demonstrated that NIRS is useful for the non-invasive diagnosis of lung cancer (Huang et al., 2003). Furthermore, NIRS is a promising technology for general cancer diagnosis, treatment decisions, and the adjustment of therapeutic drug levels (see e. g. Kondepati, Heise, and Backhaus, 2008 and Xiang et al., 2010).
- BIA for measuring body fluid volumes is widely used to diagnose adiposity (Houtkooper et al., 1996). It is now increasingly used to assess hydration in dialysis. However, for a more detailed analysis of body composition and nutritional status, further improvement and validation is necessary (Kotanko, Levin, and Zhu, 2008; Kyle et al., 2004b).

One of the key factors for making SFAs a promising tool for biomedical applications is an optimal design of the measurement setup. For example, one relevant component is the reduction of noise to obtain the best possible signal-to-noise ratio (SNR). Another important consideration is an optimal selection and placement of measurement sensors. Ideally, recorded signals should be as independent as possible to maximize information content. Improving the underlying mathematical models (such as using a full nonlinear formulation instead of simplified linear ones, see E. Haber and Oldenburg, 2000) has also been subject of research. Finally, incorporating realistic models (i. e. 3D finite element models instead of simple 2D models) into the design process can also impact modeling outcome.

1.1 Objectives

This work aims to overcome some of the specific problems in SFAs with design optimization. This in turn could further advance the field of SFAs towards an established diagnostic and therapeutic tool. Since design optimization is always domain-specific and depends on the problem at hand, the following two applications analyzed in this work will illustrate this process.

Classically, BIA tries to estimate body fat (BF) and fat free mass (FFM) using data obtained from whole-body measurements. This procedure typically relies on impedance measurement from a wrist to an ankle. However, body fat has a higher impedance than fat free tissue. Since electric current always takes the path of least resistance, adipose tissue is not the main contributing factor in this data. Thus, BIA suffers from a low sensitivity (Baumgartner, Ross, and Heymsfield, 1998). Best results are usually obtained with estimators based mainly on body mass, height, sex, and age. Obviously, ignoring impedance signals is not a satisfactory solution. Therefore, the first application in this work optimizes electrode placement close to the region of interest, incorporates the parameters of interest into the model, and applies an appropriate finite element model in simulations for the assessment of body composition with BIA (Scharfetter et al., 2005).

The second application introduces a novel method to optimize sensor placement for the illumination of highly scattering tissue such as encountered in applications of OT and photodynamic therapy (PDT). The main problem in OT is to determine the optimal location of the optical fibers, which maximizes the resolution and contrast in the region of interest (e. g. the breast or the brain). In PDT, the main challenge is to achieve a homogeneous irradiation over the whole applicator, because inhomogeneities can lead to local overdoses with serious consequences. In both of these applications, design optimization with respect to sensor positioning and magnitudes of the light sources is needed (Brunner et al., 2012).

2 Background

2.1 Interaction between matter and fields – a historical overview

2.1.1 Classical electrodynamics

The history of SFAs started as early as April 21, 1820, when Hans Christian Ørsted gave a lecture on the similarities between electric and magnetic forces at the University of Copenhagen. He believed in a fundamental connection between electric and magnetic forces and planned an experiment to show their connection. He suspected that since "the luminous and heating effect of the electrical current goes out in all directions from a conductor", it was possible that "the magnetical effect could likewise eradiate". He was "nevertheless far from expecting a great magnetical effect of the galvanical pile", but "still he supposed that a power, sufficient to make the conducting wire glowing, might be required". In his experiment, he passed a current through a very thin wire, which was placed over a compass. Ørsted prepared the experiment in advance, but an accident prevented him from trying it before the lecture. He intended to postpone the experiment, but "the probability of its success appeared stronger", so "he made the first experiment in the presence of the audience". The magnetic needle really moved, but the effect was very weak. Ørsted stated that "the experiment made no strong impression on the audience". However, Ørsted's discovery was the first step in the quest to explain the relationship between electricity and magnetism. Some ten years after his lecture, Ørsted published his findings on one of the biggest discoveries in physics (Ørsted, 1830).

In September 1820, André-Marie Ampère began to develop a mathematical and physical theory of the relationship between electricity and magnetism. In 1826, Ampère demonstrated that there is a relationship between the integrated magnetic field around a closed loop and the electric current which passes through this loop – this relationship is now famously known as Ampère's law, which he published in a memorandum in 1827 (Ampère, 1827).

The work of Ørsted and Ampère led Michael Faraday to discover electromagnetic induction in August 1831. Faraday wrapped an iron ring with two coils of insulated wire (The Royal Institution of Great Britain, 2015). When he passed a current through one coil, a corresponding current was induced in the second coil. Later on, Faraday also discovered that moving either a loop of wire or a magnet relative to each other induces an electric current in the wire. His experiments demonstrated that a changing magnetic field produces an electric field, a phenomenon now known as Faraday's law.

In 1835, the German mathematician Carl Friedrich Gauss suggested a single electrodynamic equation to describe the force between moving charges as a function of the relative velocity of the charges. This relationship is known as Gauss's law, which was published after his death in 1867 (Gauss, 1867). In a letter to his friend Wilhelm Weber, Gauss stated that he was not satisfied with his own formulation, and therefore he never published his equation: "Ich würde ohne Zweifel meine Untersuchungen längst bekannt gemacht haben, hätte nicht zur Zeit, wo ich sie abbrach, das gefehlt; was ich wie den eigentlichen Schlußstein betrachtet hatte nämlich die Ableitung der Zusatzkräfte (die zu der gegenseitigen Wirkung ruhender Elektrizitätstheile noch hinzukommen, wenn sie in gegenseitiger Bewegung sind) aus der nicht instantanen, sondern (auf ähnliche Weise wie beim Licht) in der Zeit sich fortpflanzender Wirkung. Mir hatte dies damals nicht gelingen wollen; ich verliess aber, so viel ich mich erinnere, die Untersuchung damals doch nicht ganz ohne Hoffnung, dass dies später vielleicht gelingen könnte, obwohl – erinnere ich mich recht – mit der subjektiven Überzeugung, dass es vorher nöthig sei, sich von der Art, wie die Fortpflanzung geschieht eine konstruirbare Vorstellung zu machen." Since the original quote is in German, here is a translated version: "Without a doubt, I would already have published my findings, if not the keystone would have been missing at the time when I interrupted my studies, namely the derivation of additional

forces (which are added to the mutual effects between stationary electrical particles when they are in motion), not from a non-instantaneous but (similar to the effect for light) from a time-propagating effect. At that time, I did not succeed. However, I stopped my studies (as far as I can remember) not completely without any hope that maybe I could succeed later, although – if my memory serves me well – with the subjective conviction that it would be necessary to derive a constructible concept for the mechanism behind the propagation."

At about the same time, in 1834, Heinrich Friedrich Emil Lenz formulated Lenz's law (Lenz, 1834). It states that if an electromagnetic field is generated due to a change in magnetic flux (as discovered by Faraday in 1831), the induced current produces a magnetic field which opposes the change in magnetic flux (which itself produces the current). Therefore, Lenz's law obeys the law of conservation of energy (energy cannot be created or destroyed, just transformed from one form to another), as well as Newton's third law (all forces also exist in the same magnitude and opposite direction, there are no unidirectional forces). Lenz's findings were later used by Franz Neumann, who postulated in 1845 that an electromagnetic field can be derived from a scalar and a vector potential (Neumann, 1845).

The groundbreaking work of all these researchers was finally summarized by James Clerk Maxwell in 1865. In his most fundamental work on electric impedance, Maxwell published his first set of four equations (Maxwell, 1865).

In 1881, Joseph John Thomson (who discovered the electron in 1897) derived the force for a charge q as it moves with velocity v through a magnetic field $\mathbf{B}$ – the force which we now call the "Lorentz force". Oliver Heaviside corrected Thomson's equation in 1889, because the original equation included a scaling factor of 1/2, whereas the correct scaling factor equals one (Nahin, 2002). Furthermore, Heaviside reformulated Maxwell's complete set of twenty equations (which included 18 variables) as four equations consisting of only four variables ($\mathbf{B}$, $\mathbf{E}$, $\mathbf{J}$ and ρ). For this purpose, he developed both the divergence and curl operator. Heaviside was also the first to introduce the term "impedance" in July 1886 (Heaviside, 1894).

Heinrich Rudolf Hertz worked on the experimental proof of Maxwell's theory between 1886 and 1890 (Hertz, 1892). In 1887, he confirmed the

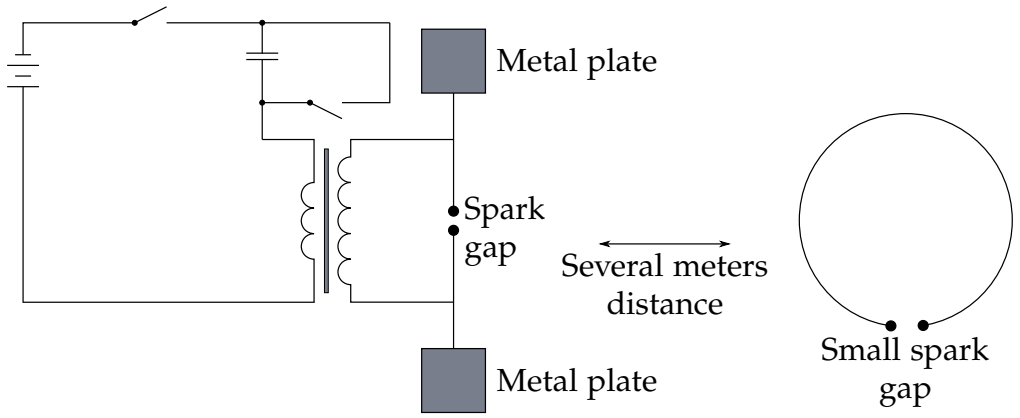

Figure 2.1: Schematic of Hertz's experiment.

existence of electromagnetic waves using an oscillator. This oscillator was connected to an induction coil and separated by a tiny gap over which a spark could leap. A receiver was placed several meters from the oscillator. As electromagnetic waves were spreading from the oscillator sparks, they induced a current in the receiver ring. This current sent sparks across the gap of the receiver ring. Hertz also discovered the photoelectric effect (published in 1887) while performing several similar experiments using different substances between the primary and secondary sparks, see Figure 2.1. Although the meaning of this effect was very obscure at that time, Hertz was still convinced that the effect was substantial for the connection between light and electricity (Scientific Biography, 2015).

At that time, the theoretical framework as well as the experimental proof of Maxwell's equations were completed, and thus the fundamental equations of EIT (see Section 2.2) – Maxwell's equations in combination with the Lorentz force – were established.

2.1.2 Radiation

A detailed history of the radiative transfer theory (RTT) is beyond the scope of this work. It is described, for example, in Johnston, 2001. The following

paragraphs provide only a brief overview of this topic.

The first publications dealing with light intensity and its measurement can be attributed to Johannes Kepler. His purely phenomenological approach led Kepler to discover the inverse square law for radiation (Kepler, 1604). After Kepler, Pierre Bouguer discovered the law now known as Beer-Lambert law (Bouguer, 1729). Additionally, he studied the scattering of light on rough surfaces. Some years later, Johann Lambert (see Lambert, 1760 or the translated version Lambert and DiLaura, 2001) introduced infinitesimals to quantitatively describe light intensity (known as radiance). He was the first to use mathematics for the interpretation of experimental results and the development of adequate mathematical models. Much later, in 1852, August Beer discovered that the absorbance of a material is proportional to the concentration of the attenuating particles in the material (Beer, 1852).

In summary, the intensity relationship known today can be attributed to Bouguer, Beer, and Lambert. The Beer-Lambert law states that the logarithm of the quantity of light received is inversely proportional to the thickness (Bouguer's contribution) and to the chemical concentration (Beer's contribution) of an absorbing material. The quantity of light is proportional to the cosine of the angle of incidence on the illuminated surface (Lambert's contribution), see e. g. Johnston, 2001.

In 1887, Eugene Lommel pioneered work on the physical and mathematical foundations of the theory of radiometry. He extended the Beer-Lambert law to include scattering (Lommel, 1889). Independently, Orest Danilowitsch Chwolson and later Arthur Schuster also developed this heuristically derived equation (Chwolson, 1889; Schuster, 1905). In 1906, Max Planck published his important theoretical definition of specific intensity (*Vorlesungen über die Theorie der Wärmestrahlung* 1906), which was later used in virtually all publications on RTT. Even though the specific intensity is only a theoretical concept, it was generally assumed that it could be calculated by solving the radiative transfer equation (RTE) and measured by a directional radiometer. Therefore, it became the central concept behind the phenomenological RTT and its applications (Mishchenko, 2013).

Although Lommel and Chwolson wrote the first publications, most authors attribute the introduction of the RTE to Arthur Schuster (Schuster, 1905) and Max Planck (Planck, 1914).

Based on Schuster's work in 1910, Jackson (Jackson, 1910) and Louis Vessot King (King, 1913) defined the RTE used in the phenomenological approach of RTT nowadays (see Lessig, Fiume, and Desbrun, 2012 and Mishchenko, 2013). Although the phenomenological and heuristic formulation of the RTT is sufficient for all subsequent considerations in this work, Richard Gans (Gans, 1924) and Subrahmanyan Chandrasekhar (Chandrasekhar, 1950) introduced the more general vector RTE, which also takes polarization of light into account. Nevertheless, numerous researchers were not satisfied that the RTT was not linked to the electromagnetic theory (see e. g. Mishchenko, 2013). The relationship between the fundamental principles of classical electrodynamics and the radiative transfer equation was not established until recently, when Michael Mishchenko published a paper which demonstrates the connection between the theories of radiative transfer and Maxwell's equations (Mishchenko, 2008).

In optical imaging (OI), a diffusion approximation of the Boltzmann transport equation (BTE) is widely used for the description of light transport in biological tissue (see e. g. Arridge, 1999). The BTE, formulated by Ludwig Boltzmann in 1872 (Boltzmann, 1970), is a nonlinear equation describing the phase space density of molecule systems that are not in equilibrium. The BTE describes the change in the density of molecules at a six-dimensional phase space point (depending on the coordinates x, y, and z, and three momentum components p_x, p_y, and p_z) at a specific time t. A profound description and historical overview can be found in Murthy, 2006.

This diffuse approximation is used because the BTE is computationally expensive. It results in relatively good approximations if the medium of interest is dominated by scattering, which is the case in most applications of OI.

2.1.3 Electromagnetic properties of biological tissue

The description of electrical properties of biological tissues goes back to 1870, when Hermann experimented with the effect of galvanic currents on muscles and nerves (Hermann, 1870). Between 1910 and 1913, Rudolf Höber proved that red blood cells and muscle cells are composed of a

conducting electrolytic interior surrounded by an insulating membrane (see Pethig and Schmueser, 2012). Höber first described the so-called beta dispersion: at low frequencies, an injected current flows around the cells, but at high frequencies it penetrates into the conductive interior. This results in a ten-fold increase in conductivity at high frequencies (around 5 MHz) as compared to low frequencies (around 150 Hz). Figure 2.2 illustrates α-dispersion, β-dispersion, and γ-dispersion.

In 1920, Philipsson measured the impedance of a suspension of red corpuscles and proposed the now well-known equivalent circuit diagram for cells (Philippson, 1920). In this model, resistance at high frequencies is much lower than at low frequencies (see Figure 2.3). Based on his work, Fricke and Morse (Fricke and Morse, 1925) determined the specific membrane capacitance of a red blood cell.

In 1928, Cole derived a general equation for the calculation of the electrical impedance of a suspension of spheres (Cole, 1928). Between 1930 and 1940, numerous publications analyzed the electrical impedances of several specific tissues, including Nitella (a type of alga) (Cole and Curtis, 1938), the squid giant axon (Curtis and Cole, 1938; Cole and Curtis, 1939), and muscle in rigor (Bozler and Cole, 1935).

In 1957, Herman Paul Schwan, often recognized as the founding father of biomedical engineering, published a seminal paper where he introduced three dispersion mechanisms for the characterization of the electric properties in biological tissue (see Schwan, 1957; Schwan, 1994).

Based on these investigations, BIA was established as a bedside routine for the determination of body composition and body hydration by the 1970s, although some problems are still to be resolved (Kyle et al., 2004a).

2.1.4 Optical properties of biological tissue

The first article dealing with the ability of light to penetrate tissue was written by Richard Bright in 1831. He introduced transillumination as a diagnostic tool for the detection of hydrocephalus (an increase of cerebrospinal fluid in the head) and intraventricular haemorrhage (Bright, 1831).

Although transillumination of tissue suffered from the diffuse nature of biological samples, applications where the effect of scattering were minimized became a useful tool in clinics. This was achieved either by examining only short path lengths (e. g. oximetry of the finger or earlobe) or by determining medical conditions which incorporate low scattering of the light source (e. g. hydrocephalus).

Optical properties of tissue have been investigated since the early 19th century, when Hasselbalch and others exposed skins to ultraviolet radiation (Duck, 2013). Optical tissue properties like transmission, absorption, and fluorescence were available by the early 1930s and can be found in general reference books such as Tuan, 2003.

Optical imaging of breast tissue (diaphanography) was first attempted by Max Cutler in 1929. He hoped to be able to distinguish between solid tumors and cysts in the breast, but had difficulties to introduce the necessary light intensity without producing extreme heat (Cutler, 1931a; Cutler, 1931b). It was not until 1990 when the diffusion approximation of the RTE (see Section 2.2.5) was sufficiently developed to accurately model tissue scattering and absorption for tomographic image reconstruction.

A significant breakthrough in optical imaging was made by Frans F. Jöbsis in 1977. He discovered the "near-infrared window", namely the wavelength range between 650 and 1350 nm, where light can penetrate tissue to a maximum depth due to low scattering (Jöbsis, 1977). This technique is known as near infrared spectroscopy (NIRS) (Gibson and Dehghani, 2009).

In 1995, the combination of multiple NIRS measurements led to the development of OT. This technique made it possible to incorporate spatial information (Gratton et al., 1995).

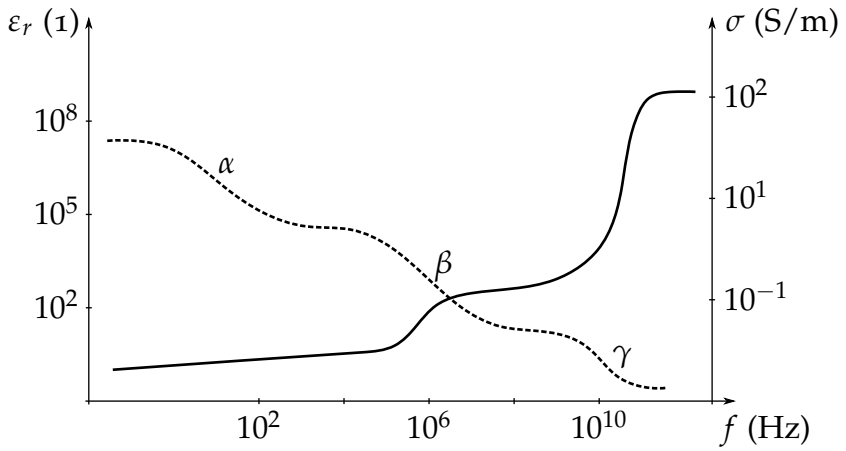

Figure 2.2: Frequency dependence of relative permittivity ε_r (dotted line) and conductivity σ (solid line) of biological tissues. Classification of α, β, and γ dispersion according to Schwan, 1957.

2.2 Physical and mathematical framework

2.2.1 Properties of biological tissue

Dielectric properties

The electromagnetic properties of biological tissue are fundamental for the description of its interactions with electromagnetic fields. These properties are affected by the structure and composition (histology) of the tissue. Measuring the impedance of biological tissue over frequency yields decreasing values when the frequency increases (see Figure 2.2). This frequency dependence arises from several mechanisms which occur at different frequency ranges (see e. g. Foster and Schwan, 1995). The dispersion is the transition from one level of relative permittivity to another, and its characteristic frequency f_c is the frequency at which the mean value between these ε_r levels occurs.

The most important frequency domain for BIA is the beta dispersion between 10^4 and 10^8 Hz. There are numerous models for the description of the frequency dependence within this frequency domain, and arguably the

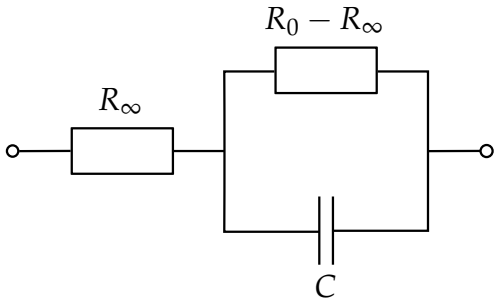

Figure 2.3: Equivalent circuit for tissues and compacted red blood cells as developed by Philippson, 1920. R_∞ and R_0 are the resistances of the tissue at high and low frequencies, respectively. C is the membrane capacitance.

most popular one for biological tissue is the Cole model (Cole, 1940). This model describes the frequency dependence of the impedance based on an equivalent electrical circuit.

The Cole equation is based on the assumption that biological tissue is composed of extracellular and intracellular liquid volumes (see Figure 2.4). An electric current mainly passes through the extracellular fluid at low frequencies, because the lipid cell membrane is an insulator which prevents the current to enter the cells. At high frequencies, the current can penetrate the cell membrane and passes through both the extra- and intracellular fluids. Consequently, the overall impedance drops.

As there are no inductive effects in biological tissue, the magnitude of the tissue impedance can be formulated as $|Z| = \sqrt{R^2 + X_C^2}$, and the phase angle is equal to $\phi = -\arctan(\frac{X_C}{R})$. Here, R is the the resistance, and X_C is the reactance caused by the capacitance C of the cell membrane.

In 1940, Kenneth Cole developed an equation which describes the dispersion of the impedance Z in biological tissue (Equation 2.1). Here, R_∞ is the resistance of the tissue at high frequencies, R_0 is the resistance at low frequencies, and $\tau = \frac{1}{2\pi f_c}$ is the relaxation time (with f_c being the characteristic frequency). The Cole exponent α is chosen in such a way that the simulated values approximate the measurement data optimally.

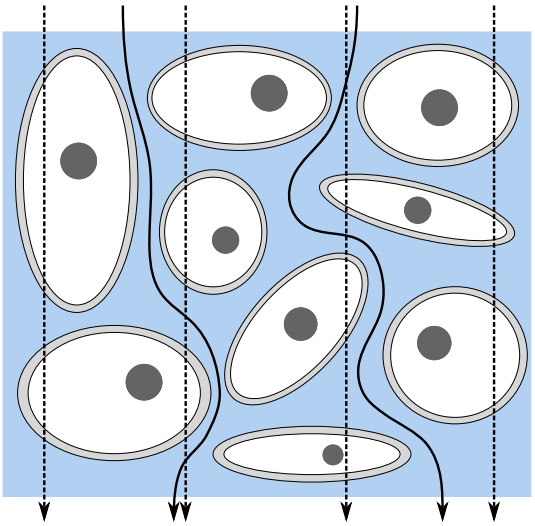

Figure 2.4: Electric current flow through biological tissue. Solid lines indicate current flow at low frequencies, and dashed lines at high frequencies.

$$Z(\omega) = R_\infty + \frac{R_0 - R_\infty}{1 + (j\omega\tau)^\alpha} \tag{2.1}$$

Usually, the electrical properties of biological tissues are described in terms of the electrical conductivity σ, the permittivity $\varepsilon = \varepsilon_0\varepsilon_r$, and the magnetic permeability $\mu = \mu_0\mu_r$. The first of these properties not only depend on tissue type, but also on frequency, as can be seen in Figure 2.2. The last property, μ, is almost the same as in free space for all tissue types and does not depend on frequency. A detailed description of all these properties can be found in Section 2.2.3, their units are given in Table 2.1.

Optical properties

The first step towards an optimal design of therapeutic or diagnostic applications is to specify the optical properties of a tissue. The second step is to use these optical properties in an appropriate light transport model to estimate light distribution (Jacques, 2013). When describing photon transport in biological tissue, some parameters are particularly interesting: the

Table 2.1: Electrical parameters and their description.

Parameter	Description	Unit
σ	Electrical conductivity	S/m
ε	Dielectric constant or permittivity	F/m
ε_0	Dielectric constant of free space	$8.8542 \cdot 10^{-12}$ F/m
μ	Magnetic permeability	H/m
μ	Magnetic permeability of free space	$4\pi \cdot 10^{-7}$ H/m
κ	Complex conductivity	S/m

reflection coefficient, the scattering coefficient, the scattering phase function, and the absorption coefficient (see Table 2.2 for more details).

Table 2.2: Optical parameters and their description.

Parameter	Description	Unit
R	Reflection coefficient	1
μ_s	Scattering coefficient	cm^{-1}
$p(\hat{\mathbf{s}}, \hat{\mathbf{s}}')$	Scattering phase function	sr^{-1}
μ_a	Absorption coefficient	cm^{-1}

Reflection can be predicted by the Fresnel equations (which can be derived using Maxwell's equations). These equations describe how much light penetrates into biological tissue and how much is reflected back.

Scattering in biological tissue occurs manly due to the presence of cells, nuclei, mitochondria, and other components. These scatterers are distributed randomly in biological tissue, and the induced photons usually encounter multiple scattering events before they are absorbed or transmitted out of the probe. The scattering coefficient μ_s is is the average number of scattering events per distance. Accordingly, the scattering mean free path is the inverse of the scattering coefficient. Scattering is angle dependent which is considered using the scattering phase function $p(\hat{\mathbf{s}}, \hat{\mathbf{s}}')$. This function describes the angular distribution of light intensity scattered by a particle

at a given wavelength. In this function, $\hat{\mathbf{s}}$ is the unit vector of the photon's original direction and $\hat{\mathbf{s}}'$ the unit vector of its new direction. In biological tissue, scattering is the dominating factor as compared to absorption. Thus, an average parameter $g = \langle \cos\theta \rangle$, the anisotropy factor of scattering, is used to characterize tissue scattering. This factor gives the mean amount of forward direction retained after a single scattering event. In this equation, θ is the angle between the incident and scattered directions. The anisotropy factor g can be any value between -1 and 1, where -1 characterizes strong backscattering. If $g = 0$, the phase function is isotropic, whereas large values of g indicate anisotropic phase functions. In diffuse media, the reduced scattering coefficient $\mu_s' = \mu_s(1-g)$ is often used.

Absorption in biological tissue occurs mainly due to water, melanin, lipids, and blood. The absorption coefficient μ_a can be defined in terms of the probability of a photon being absorbed: the probability that a photon will be absorbed while traveling a distance of $z + fa\partial z$ is $\mu_a \partial z$. The absorption mean free path is the inverse of the absorption coefficient. After absorption, a molecule is no longer in its ground state, but in an excited state. There are four possibilities which may occur next: ionization, chemical reaction, thermalization or radiative emission. Ionization and chemical reaction usually occur with ultraviolet or gamma radiation, because they require high energies. Thermalization occurs when the energy of the excited electron is dissipated increasing the kinetic energy of the structures involved (non-radiative transfer). The last possibility is the abrupt emission of energy via radiation, where two possible forms can occur: fluorescence and phosphorescence. Both of these effects can occur in PDT (see Figure 2.5) and are therefore described in detail in Section 2.2.2.

The sum of the absorption and scattering coefficients is the total attenuation coefficient $\mu_t = \mu_a + \mu_s$. In the diffusion approximation, the transport attenuation coefficient $\mu_{tr} = \mu_a + \mu_s'$ or the optical diffusion coefficient $\kappa = \frac{1}{3(\mu_a + \mu_s')}$ are often used instead. Here, $\mu_s' = (1-g)\mu_s$ is the reduced scattering coefficient already mentioned above, which incorporates the anisotropy factor g into the scattering coefficient μ_s. For biological tissues, this factor usually has a value of -0.9.

2.2.2 Photodynamic therapy

PDT is a minimally invasive therapeutic procedure which uses a photosensitizer in combination with light of a specific wavelength. In the presence of normal oxygen O_2, PDT produces singlet oxygen O_2^*, which kills nearby cells by either causing apoptosis or necrosis. Additionally, PDT can damage blood vessels in a tumor and thus cut off the nutritional supply for the cancer cells (Agostinis et al., 2011).

Figure 2.5 illustrates the process of producing singlet oxygen. Normally, the photosensitizer (PS) is in its ground state with two electrons having opposite spin in a low energy molecular orbital (most often, this is the singlet state). Absorbing energy (a photon) from the light source transfers one electron of the PS to a high-energy orbital, but it keeps its spin from the singlet state. This excited PS is unstable and has two possible subsequent reactions: it either emits its excess energy through fluorescence and/or heat (within a few nanoseconds), or it undergoes intersystem crossing, where the spin of the excited electron inverts to a more stable triplet state that has electrons which spin in parallel.

This excited triplet state PS is stable and can lose its energy through phosphorescence (within milliseconds, seconds or even hours), or it undergoes one of two possible reactions – a Type I reaction or a Type II reaction. In a Type I reaction, the PS transfers an electron to a molecule and forms hydroxyl radicals. These radicals may then react with oxygen and produce free radicals. In a Type II reaction, which is the main process occurring in PDT, the excited triplet PS transfers its energy to a ground-state triplet oxygen molecule and yields the non-radical but highly reactive singlet oxygen. Both reaction types occur simultaneously with a probability ratio depending on the PS type used, the substrate, and oxygen concentrations.

PDT is designed to be as selective as possible. This is achieved by two facts: photosensitizers are preferentially absorbed by cancerous tissue, and the light source is focused directly to the target tissue. Then, the high reactivity and short half-life of singlet oxygen and reactive oxygen species guarantees the locally restricted cell destruction. On the one hand, this localization is necessary, but on the other hand it is also one of the limitations of PDT

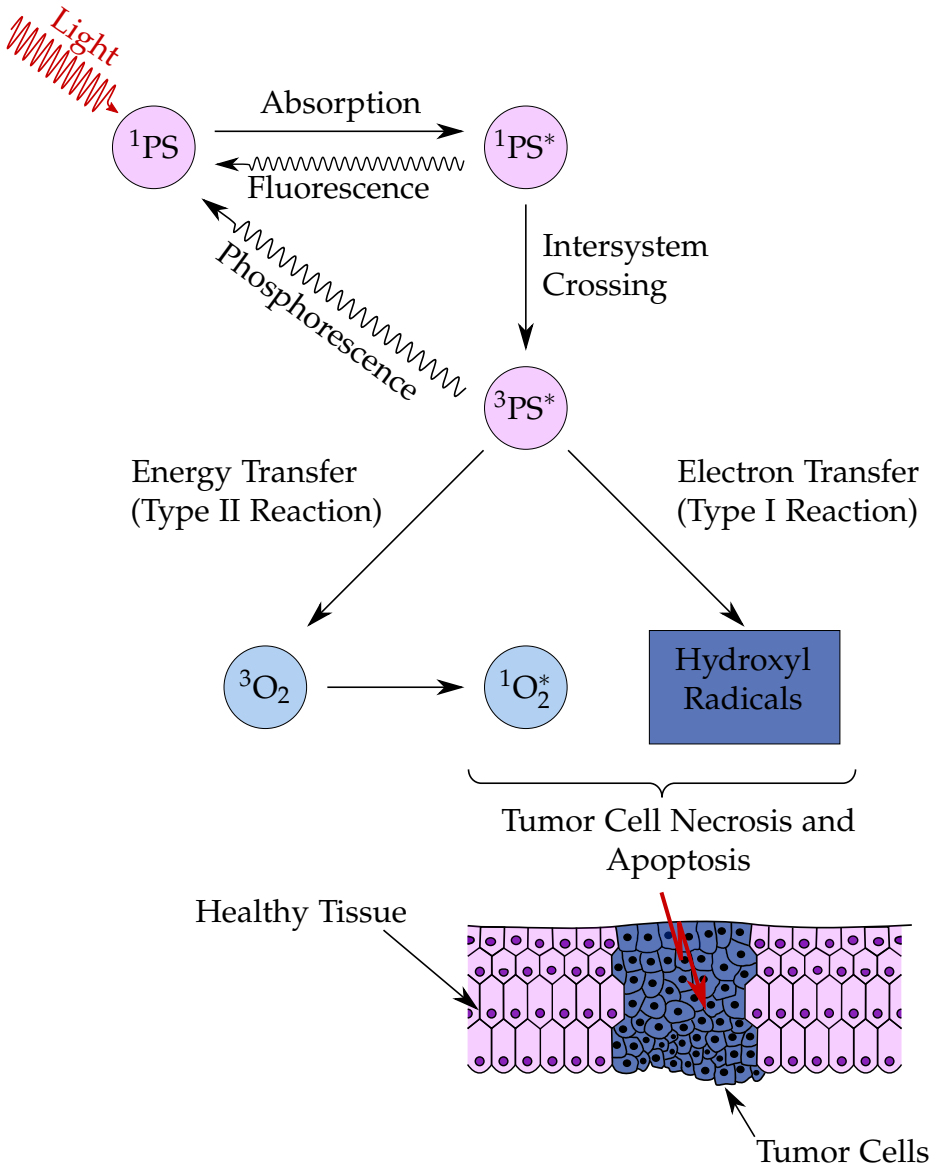

Figure 2.5: Processes involved in photosensitization: Light exposure takes the PS molecule from the ground singlet state (^{1}PS) to an excited singlet state (^{1}PS*). This PS now either emits its excess energy through fluorescence and/or heat or it undergoes intersystem crossing and becomes an excited PS in triplet state (^{3}PS*). This excited triplet state PS can lose its energy through phosphorescence or it undergoes a Type I or Type II reaction. The Type I reaction produces hydroxyl radicals, whereas the Type II reaction produces free radicals ($^1O_2^*$). These radicals then result in tumor cell death (necrosis and apoptosis).

because it is the reason why PDT is inefficient against metastases, which are the most common causes of death for cancer patients.

PDT is used as a supplement to other therapies like surgery, chemotherapy, radiotherapy, or immunotherapy and can be utilized either after or before these therapies.

The requirements for photosensitizers used in PDT are a high absorption between 600 and 800 nm (photons with wavelengths longer than 800 nm do not excite oxygen to its singlet state), no dark toxicity, and rapid clearance from healthy tissue to minimize phytotoxic side effects (see e. g. Allison and Sibata, 2010).

The optical window of tissue lies between 600 and 1200 nm, but light with wavelengths greater than 800 nm does not have enough energy to initiate a photodynamic reaction to produce oxygen in singlet state. Therefore, the wavelengths used in PDT lie between 600 and 800 nm. This also limits the possible treatment depth to approximately one centimeter. The optimal choice of the wavelength depends on the localization, size, and tissue characteristics of the tumor tissue as well as the absorption of the photosensitizer. Most often, light-emitting diodes or laser diodes are used in PDT, because they show narrow spectral bandwidths and high fluence rates (Juzeniene et al., 2004; Brancaleon and Moseley, 2002).

Although PDT is a promising emerging technique, which has been applied for the treatment of various tumors (including esophagel, skin, lung, liver, bladder, prostate, head, and neck tumors), there are several technical difficulties in its application. Many publications mention that an improved light delivery may propel PDT to the forefront of oncological treatment, because it is an inexpensive solution and might even be able to reduce the necessity for surgery (Lim et al., 2013).

2.2.3 Maxwell's equations

A basic understanding of the relations between the passive electrical properties and the electromagnetic field is essential for the development of BIA, EIT and MIT. Therefore, the objective of this chapter is to provide an overview

of Maxwell's equations and their connection with the electrical properties of a material, based on the more detailed book (Huray, 2010) . Table 2.3 summarizes the variables and their description used in this work.

Table 2.3: Variables and their description for Maxwell's equations.

Variable	Description	Unit
E	Electric field strength	V/m
D	Electric flux density	C/m^2
H	Magnetic field strength	A/m
B	Magnetic flux density	Wb/m^2
ρ	Electric charge density	C/m^3
σ	Conductivity	S/m
ε	Permittivity	F/m
μ	Permeability	H/m

The first Maxwell Equation is defined as

$$\nabla \cdot \mathbf{D} = \rho. \tag{2.2}$$

It describes Gauss's law at any point in space. For three-dimensional cartesian coordinates, the nabla operator ∇ can be rewritten as

$$\nabla := \begin{pmatrix} \frac{\partial}{\partial x} \\ \frac{\partial}{\partial y} \\ \frac{\partial}{\partial z} \end{pmatrix}. \tag{2.3}$$

Thus, the left hand-side of the first Maxwell equation can be written as

$$\nabla \cdot \mathbf{D} = \begin{pmatrix} \frac{\partial}{\partial x} \\ \frac{\partial}{\partial y} \\ \frac{\partial}{\partial z} \end{pmatrix} \cdot \begin{pmatrix} D_x(x,y,z) \\ D_y(x,y,z) \\ D_z(x,y,z) \end{pmatrix} = \frac{\partial}{\partial x} D_x + \frac{\partial}{\partial y} D_y + \frac{\partial}{\partial z} D_z, \tag{2.4}$$

which results in a scalar value, the electric charge density ρ. This equation states that if there exists an electric charge, the divergence of **D** is not equal to zero at this point. Therefore, the electric field lines always extend from

positive charges to negative charges. For single charges, they extend to infinity.

When relating the electric flux density to the electric field using $\mathbf{D} = \varepsilon \cdot \mathbf{E}$, one of the passive material properties comes into play, the permittivity $\varepsilon = \varepsilon_0 \cdot \varepsilon_r$ (where $\varepsilon_0 = 8.8541 \cdot 10^{-12}\,\mathrm{F/m}$ is the vacuum permittivity). When a material (which possesses a permanent or an induced electric dipole moment) is placed in between two charged plates, the electric field inside the plates $\mathbf{E}$ decreases. This is because the molecules will be aligned by the electric field. The alignment will be opposed to the external electric field $\mathbf{E}$, resulting in a reduction of $\mathbf{E}$. How much a material will reduce the external electric field is measured by the relative permittivity ε_r.

The second Maxwell Equation is defined as

$$\nabla \cdot \mathbf{B} = 0. \tag{2.5}$$

Maxwell's second equation deals with magnetic fields, whereas his first equation involves electric fields. Both equations are almost symmetrical except for the quantity on the right-hand side. In analogy to the first equation, it would be tempting to state that the divergence of the magnetic flux density $\mathbf{B}$ is equal to the (hypothetical) magnetic charge density. However, nobody has found magnetic charges or magnetic monopoles so far. Therefore, magnetic fields always form a closed loop. This is what the second Maxwell equation, often called Gauss's law for magnetism, states.

Similar to the first equation, we can relate the magnetic field $\mathbf{H}$ to the magnetic flux density $\mathbf{B} = \mu \cdot \mathbf{H}$. Here, μ is the permeability of a material, which measures how easily a magnetic field can pass through the material. In analogy to the permittivity, it is defined as $\mu = \mu_0 \cdot \mu_r$, where μ_0 is the vacuum permeability and μ_r the relative permeability of the material.

Faraday's law is the third Maxwell equation:

$$\nabla \times \mathbf{E} = -\frac{\partial \mathbf{B}}{\partial t} \tag{2.6}$$

This law states that a time-varying magnetic field generates an electric field.

Maxwell's fourth equation is called Ampère's law:

$$\nabla \times \mathbf{H} = \mathbf{J} + \frac{\partial \mathbf{D}}{\partial t} \tag{2.7}$$

Before Maxwell formulated this equation, Ampère's law was written as $\nabla \times \mathbf{H} = \mathbf{J}$. If that was true, $\nabla \cdot (\nabla \times \mathbf{H}) = \nabla \cdot \mathbf{J}$, but since the divergence of the curl is always zero for any vector field $\mathbf{X}$ (i. e. $\nabla \cdot (\nabla \times \mathbf{X}) = 0$), the divergence of $\mathbf{J}$ would be equal to zero. Obviously, this is not true, because it would imply that the electric current flowing into any region is always equal to the current flowing out of that region. However, when integrating over one side of a capacitor, this assumption does not hold. Therefore, Maxwell added the displacement current density $\mathbf{J}_d = \frac{\partial \mathbf{D}}{\partial t}$ to Ampère's law. In summary, Maxwell's fourth equation shows that an electric current produces a magnetic field that circles around the current. Additionally, a time-varying electric flux density also results in a magnetic field. Hereby, $\mathbf{J}$ is the electric current density and can be related to the electric field using Ohm's Law $\mathbf{J} = \sigma \cdot \mathbf{E}$. The electrical conductivity σ gives the amount of current flow for a given electric field and it is the analogy of the inverse of the resistance in an electric circuit.

Putting together all four equations, we now know that a time-varying magnetic flux density results in an electric field. A time-varying electric flux density itself gives rise to an magnetic field and so forth. This is the origin of electromagnetic waves, which propagate at the speed of light.

2.2.4 Fundamental equation of impedance measurements

Maxwell's equations (see Section 2.2.3) are the basis of EIT. For BIA and EIT, electrostatic conditions are assumed. This means that all electric charges are assumed to be stationary or moving very slowly, and thus there are no magnetic forces between them. It also implies that the third Maxwell equation $\nabla \times \mathbf{E} = -\frac{\partial \mathbf{B}}{\partial t}$ reduces to

$$\nabla \times \mathbf{E} = 0. \tag{2.8}$$

We can introduce a magnetic vector potential $\mathbf{A}$, defined by the magnetic field $\mathbf{B}$, and the electric scalar potential ϕ. The magnetic vector potential $\mathbf{A}$ can be defined as

$$\mathbf{B} = \nabla \times \mathbf{A}, \tag{2.9}$$

and because

$$\nabla \cdot \mathbf{B} = \nabla \cdot (\nabla \times \mathbf{A}), \tag{2.10}$$

this magnetic vector potential must always exist (the right hand side is always equal to zero and thus the second Maxwell equation is always fulfilled).

The electric field $\mathbf{E}$ can then be defined using the electric scalar potential ϕ and the magnetic vector potential $\mathbf{A}$ as

$$\mathbf{E} = -\nabla\phi - \frac{\partial \mathbf{A}}{\partial t}. \tag{2.11}$$

When neglecting the effect of magnetic induction (electrostatic conditions), this equation simplifies to

$$\mathbf{E} = -\nabla\phi. \tag{2.12}$$

Using Maxwell's fourth equation and neglecting current sources within the object, we get

$$\nabla \times \mathbf{H} = \kappa\mathbf{E}. \tag{2.13}$$

Taking the divergence on both sides, this yields

$$\begin{aligned} \nabla \cdot (\nabla \times \mathbf{H}) &= \nabla \cdot (\kappa\mathbf{E}) \\ 0 &= \nabla \cdot (\kappa(-\nabla\phi)). \end{aligned} \tag{2.14}$$

Thus we obtain $\nabla \cdot (\kappa\nabla\phi) = 0$, the fundamental equation for EIT and BIA (see e. g. Cheney, Isaacson, and Newell, 1999). This nonlinear (in kappa) partial differential equation has an infinite number of solutions and therefore boundary conditions are required to restrict these. Usually, these boundary conditions are the potential at the surface (Dirichlet conditions), the current density crossing the boundary (Neumann conditions) or a mixture of these two. The inverse problem of EIT reconstructs the conductivity distribution inside the body using multiple measurements of the potential on the body's surface.

2.2.5 Radiative transfer equation

As already alluded to in Chapter 2.1.2, Mishchenko, 2008 recently established the link between the originally heuristically derived radiative transfer equation and Maxwell's equations. However, for practical use, the heuristically derived model for the photon transport is sufficient and given by the RTE in Equation 2.15.

$$\frac{1}{c}\frac{\partial}{\partial t}\phi(\mathbf{r},\hat{\mathbf{s}},t) + \hat{\mathbf{s}}\nabla\phi(\mathbf{r},\hat{\mathbf{s}},t) + (\mu_s+\mu_a)\phi(\mathbf{r},\hat{\mathbf{s}},t) = \\ = \mu_s\int_{4\pi} p(\hat{\mathbf{s}},\hat{\mathbf{s}}')\phi(\mathbf{r},\hat{\mathbf{s}}',t)d\hat{\mathbf{s}}' + Q(\mathbf{r},\hat{\mathbf{s}},t) \tag{2.15}$$

In this equation, $\phi(\mathbf{r},\hat{\mathbf{s}},t)$ is the radiance or angular flux of photons, where $\mathbf{r}$ is the spatial position, $\hat{\mathbf{s}}$ the unit direction, and t the time point.

The second term, $\hat{\mathbf{s}}\nabla\phi(\mathbf{r},\hat{\mathbf{s}},t)$, describes the loss through the boundary, and $(\mu_s+\mu_a)\phi(\mathbf{r},\hat{\mathbf{s}},t)$ the loss due to scattering and absorption phenomena. On the right hand side, the two terms describing the involved gains are given: $\mu_s\int_{4\pi} p(\hat{\mathbf{s}},\hat{\mathbf{s}}')\phi(\mathbf{r},\hat{\mathbf{s}},t)d\hat{\mathbf{s}}'$ describes the amount of photons gained through scattering from any direction $\hat{\mathbf{s}}'$ into the direction $\hat{\mathbf{s}}$, and the last term, $Q(\mathbf{r},\hat{\mathbf{s}},t)$, describes the injected power. The scattering and absorption coefficients are given by μ_s and μ_a, and $p(\hat{\mathbf{s}},\hat{\mathbf{s}}')$ is the scattering phase function, which describes the angular dependence of light scattering by a particle at a given wavelength.

For the description of light propagation in biological tissue, the diffusion approximation of the radiative transfer equation is used, because the complete model of photon transport can only be solved with Monte Carlo simulations, which is computationally expensive. The assumptions when using this approximation are summarized below.

The complete RTE incorporates six independent variables: x, y, and z from the spatial position $\mathbf{r}$, the polar angle θ and the azimuthal angle ϕ from $\hat{\mathbf{s}}$, and the time point t. In a scattering medium (as opposed to media with high absorption), the number of variables can be reduced to only four variables by assumptions known as diffusion theory for photon transport.

Table 2.4: Variables and their description for the radiative transfer equation.

Variable	Description	Unit
$\phi(\mathbf{r}, \hat{\mathbf{s}}, t)$	Radiance or angular flux of photons	$\mathrm{Wm}^{-2}\mathrm{sr}^{-1}$
$\mathbf{r}$	Spatial position	1
$\hat{\mathbf{s}}$	Unit direction of interest	1
$\hat{\mathbf{s}}'$	Unit scattering direction	1
t	Time point	1
μ_a	Absorption coefficient	cm^{-1}
μ_s	Scattering coefficient	cm^{-1}
$p(\hat{\mathbf{s}}, \hat{\mathbf{s}}')$	Scattering phase function	sr^{-1}

The purpose of the diffusion approximation is to remove any unnecessary complications to obtain a model which is simple enough to solve. If the angular dependence of light varies only slowly, i. e., if the difference between the radiance $\phi(\hat{\mathbf{s}})$ and $\phi(\hat{\mathbf{s}} + \Delta\hat{\mathbf{s}})$ is small, the RTE can be simplified. One way is to express the directional dependence as a sum of N spherical harmonics which leads to the well known family of P_N approximations. One of this set of approximations, the P_1 approximation, is used for the diffusion approximation of the RTE (see e. g. Arridge, 1999). Therefore, the RTE (Equation 2.15) is first integrated over all angles, and then multiplied by $\hat{\mathbf{s}}$, and integrated over all angles (see Cox, 2014). For the calculation of the P_1 approximation, two quantities are very useful: the fluence rate and the flux vector.

The fluence rate is the radiance integrated over all directions $\hat{\mathbf{s}}$:

$$\Phi(\mathbf{r}, t) = \int_0^{4\pi} \phi(\mathbf{r}, \hat{\mathbf{s}}, t) d\hat{\mathbf{s}}.$$

The flux vector is the direction-weighted radiance, integrated over all directions $\hat{\mathbf{s}}$:

$$\mathbf{F}(\mathbf{r}, t) = \int_0^{4\pi} \hat{\mathbf{s}}\phi(\mathbf{r}, \hat{\mathbf{s}}, t) d\hat{\mathbf{s}}.$$

When integrating the RTE over all angles, the five terms become:

$$\int_{4\pi} \frac{\partial \phi(\mathbf{r}, \hat{\mathbf{s}}, t)}{\partial t} d\hat{\mathbf{s}} = \frac{\partial \Phi(\mathbf{r}, t)}{\partial t}$$

$$\int_{4\pi} \hat{\mathbf{s}} \nabla \cdot \phi(\mathbf{r}, \hat{\mathbf{s}}, t) d\hat{\mathbf{s}} = \nabla \cdot \mathbf{F}(\mathbf{r}, t)$$

$$\int_{4\pi} (\mu_s + \mu_a) \phi(\mathbf{r}, \hat{\mathbf{s}}, t) d\hat{\mathbf{s}} = (\mu_a + \mu_s) \Phi(\mathbf{r}, t)$$

$$\int_{4\pi} \mu_s \int_{4\pi} p(\hat{\mathbf{s}}, \hat{\mathbf{s}}') \phi(\mathbf{r}, \hat{\mathbf{s}}', t) d\hat{\mathbf{s}}' d\hat{\mathbf{s}} = \mu_s \Phi(\mathbf{r}, t)$$

$$\int_{4\pi} Q d\hat{\mathbf{s}} \equiv q_0$$

Summarizing all these terms gives:

$$\frac{1}{c} \frac{\partial \Phi(\mathbf{r}, t)}{\partial t} + \nabla \cdot \mathbf{F}(\mathbf{r}, t) + \mu_a \Phi(\mathbf{r}, t) = q_0 \tag{2.16}$$

When multiplying by $\hat{\mathbf{s}}$ and integrating over all angles, the five terms of the RTE become:

$$\int_{4\pi} \hat{\mathbf{s}} \frac{\partial \phi(\mathbf{r}, \hat{\mathbf{s}}, t)}{\partial t} d\hat{\mathbf{s}} = \frac{\partial \mathbf{F}(\mathbf{r}, t)}{\partial t}$$

$$\int_{4\pi} \hat{\mathbf{s}} (\hat{\mathbf{s}} \nabla \cdot \phi(\mathbf{r}, \hat{\mathbf{s}}, t)) d\hat{\mathbf{s}} = \frac{1}{3} \nabla \Phi(\mathbf{r}, t)$$

$$\int_{4\pi} \hat{\mathbf{s}} (\mu_a + \mu_s) \phi(\mathbf{r}, \hat{\mathbf{s}}, t) d\hat{\mathbf{s}} = (\mu_a + \mu_s) \mathbf{F}(\mathbf{r}, t)$$

$$\int_{4\pi} \hat{\mathbf{s}} \mu_s \int_{4\pi} p(\hat{\mathbf{s}}, \hat{\mathbf{s}}') \phi(\mathbf{r}, \hat{\mathbf{s}}', t) d\hat{\mathbf{s}}' d\hat{\mathbf{s}} = g \mu_s \mathbf{F}(\mathbf{r}, t)$$

$$\int_{4\pi} \hat{\mathbf{s}} q d\hat{\mathbf{s}} = q_1$$

Here, q_1 is an anisotropic source. Summarizing all these terms gives:

$$\frac{1}{c} \frac{\partial \mathbf{F}(\mathbf{r}, t)}{\partial t} + \frac{1}{3} \nabla \cdot \Phi(\mathbf{r}, t) + (\mu_a + \mu_s) \mathbf{F}(\mathbf{r}, t) = g \mu_s \mathbf{F}(\mathbf{r}, t) + q_1 \tag{2.17}$$

The combination of Equations 2.16 and 2.17 is called the P_1 approximation. This approximation assumes that the expansion of the radiance is limited to

the first-order spherical harmonics. This can be interpreted as a radiance which is almost isotropic. The second approximation is that the change in photon flux is much lower than the photon collision frequency (i. e. scattering occurs much more frequently than absorption).

Assuming that $\frac{\partial \mathbf{F}}{\partial t} \approx 0$, neglecting all anisotropic sources ($q_1 = 0$), and introducing the diffusion coefficient $\kappa = \frac{1}{3(\mu_a + \mu_s')}$, Equation 2.17 can be rearranged and written as

$$\mathbf{F} = -\kappa \nabla \Phi. \tag{2.18}$$

Substituting Equation 2.18 into 2.16 gives the diffusion approximation of the RTE:

$$\frac{1}{c}\frac{\partial \Phi}{\partial t} - \nabla \cdot \kappa \nabla \Phi + \mu_a \Phi = q_0. \tag{2.19}$$

Here, κ is the diffusion coefficient, μ_a the absorption coefficient, c the speed of light, $\mu_s' = \mu_s(1 - g)$ the reduced scattering coefficient, and g is the anisotropy factor of scattering (see also Section 2.2.1).

The forward problem of diffuse optical tomography (DOT) is the computation of the light fluence on a boundary of a tissue with specific and known optical properties. There are several approaches for the solution of the forward problem of DOT. Since analytical solutions only exist for simple geometries like spheres, they cannot be used in most real world setups. Monte Carlo simulations stochastically simulate the propagation of individual photons until they are absorbed in the tissue or exit the boundary (Wang, Jacques, and Zheng, 1995). As this method is computationally demanding, in this work the finite element method (FEM) is used instead (see e. g. Dhatt, Lefrançois, and Touzot, 2012). It solves the transport equation on a discretized domain. The discretization is usually done by segmenting CT or MRI images and creating meshes. A mesh is composed of nodes, whereby four nodes form tetrahedral elements. A connection of numerous elements with their volumes and surfaces form the individual three-dimensional FEM. The solution of the diffusion approximation of the RTE is expressed in terms of piecewise linear basis functions. That way, a smooth solution for the corresponding photon density distribution inside the mesh is guaranteed.

3 Fat and hydration monitoring using bioimpedance analysis

3.1 Introduction

Assessing the human body composition, in particular quantifying the percentage of fat free mass (FFM) and body fat (BF) in different compartments, is important in different disciplines like sports sciences, clinical nutrition, assessment of the nutritional condition of the aging population, and management of obesity. Obesity is an increasing problem not only in the USA and Europe but also in developing nations such as Asia and Africa (Bhurosy and Jeewon, 2014). The prevalence of overweight and obesity has also increased among children (Wang and Lobstein, 2006). It is connected to health risks like coronary heart disease, high blood pressure, stroke, type 2 diabetes, and more (DeFronzo et al., 2014). BIA is a cheap, safe, non-invasive, and painless method to analyze body composition, and thus an improvement of its reliability would be desirable to transform it into a useful tool in clinical practice.

Currently, hydrostatic weighing is one of the gold standards for the assessment of BF. When compared to hydrostatic weighing, BIA shows standard errors between 2 % and 5 % of the total body mass. These errors seem low at first glance, but considering an average weight of 70 kg, this translates to an error of 1.4 to 3.5 kg. BF usually ranges from 5 % to 40 % (which is 3.5 to 40 kg for a person weighing 70 kg). This implies that the relative errors can become quite large especially for slim subjects (Baumgartner, Chumela, and Roche, 1989; Segal et al., 1988; Lukaski, 1987; McNeill et al., 1991; Organ et al., 1994; Baumgartner, Ross, and Heymsfield, 1998).

In BIA, the current mainly passes through highly conducting fat-free regions, so the direct sensitivity of the BF parameter is low. Fat contributes significantly to the overall conductance only in considerably obese people – in all other cases, muscle is the main conductor (Baumgartner, Ross, and Heymsfield, 1998). Therefore, BF is usually directly derived from the estimated FFM, but errors propagate and make BIA sensitive to interferences. For example, changes in the water content of the FFM or redistribution of body fluids (e. g. due to orthostatic processes) can result in considerable errors. Furthermore, since the trunk only contributes 5 % to 10 % to the total impedance, conventional whole body BIA measurements contain little information about abdominal fat. Leg to leg and arm to arm measurements obviously cannot perform better. Therefore, a more direct method with high sensitivity to adipose tissue in central body compartments is required.

This work tries to overcome one of the current problems in BIA. Usually, the BF is estimated by subtracting the FFM (which is negatively correlated with the measured impedance) from the whole body mass. To reduce the poor correlation between measured impedance and estimated BF, most estimators include anthropometric data such as body mass, height, sex, and age in their calculations. As a matter of fact, the best reproducibility is obtained with estimators which put a relatively low weight on measured impedance (Kyle et al., 2004a). This is very unsatisfactory, because the impedance measurements do not add as much diagnostic information as they theoretically contain.

Intuitive quantities of interest for the assessment of human body composition are the subcutaneous fat mass and the fraction of adipose tissue in the muscular and mesenteric compartments. However, these quantities are not directly measurable using impedance measurements. The only accessible parameter is the frequency dependence of the impedance, which itself is created by the frequency dependence of the conductivities (conductivity spectra) of all involved tissues. These conductivity spectra contain information about microstructural properties like the hydration state.

The first step toward an improved sensitivity of the measured impedance on the BF parameter is a redesign of the measurement setup for BIA (see Figure 3.1). As suggested in Scharfetter et al., 2001, a local measurement of abdominal transimpedance yields more accurate information about central

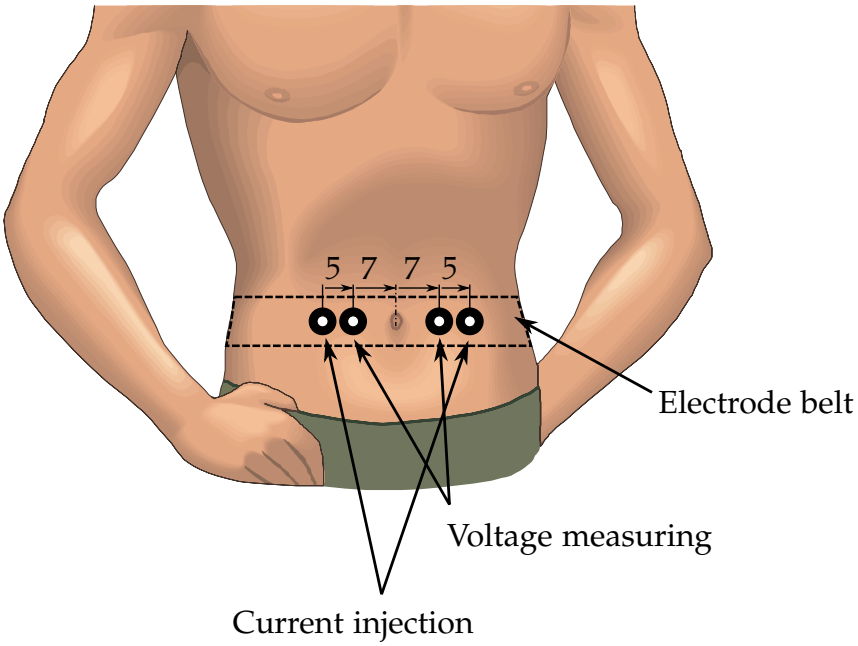

Figure 3.1: Measurement configuration. Location and spacing of the voltage measuring and current injection electrodes with inter-electrode distances (in cm). Modified from Scharfetter et al., 2005.

fat compartments, because the electrical field is focused on the region of interest. This is due to the fact that the current has to pass through both the FFM and the BF within the abdomen. The potential difference measured on the surface is then determined by the local geometry and the local composition of the different tissue layers. This is also a significant advantage over traditional whole body BIA – the abdominal transimpedance is highly sensitive to the local fat content and insensitive to fluid shifts far away in the extremities.

Scharfetter et al., 2001 defined the subcutaneous fat layer thickness (SFL) as the thickness of the fat below one of the voltage measuring electrodes (illustrated in Figure 3.2).

It has been shown that the values of the SFL are strongly linearly correlated with the abdominal electrical impedance (Scharfetter et al., 2001). Figure 3.3 shows published data from (Scharfetter et al., 2001) for a current injection

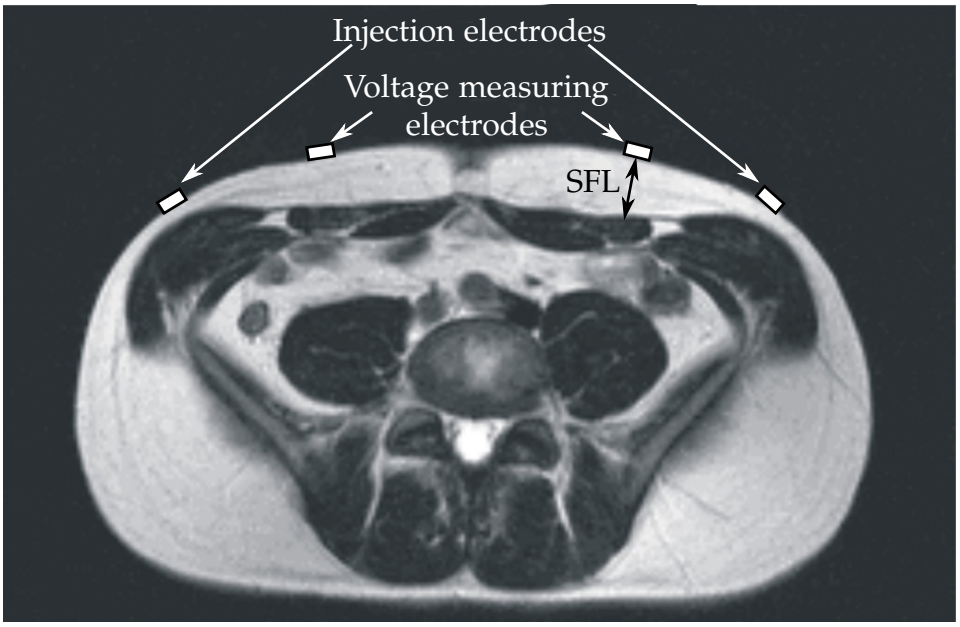

Figure 3.2: Magnetic resonance image showing the positions of current injection and voltage measuring electrodes as well as the definition of the subcutaneous fat layer thickness (SFL). Modified from Scharfetter et al., 2005.

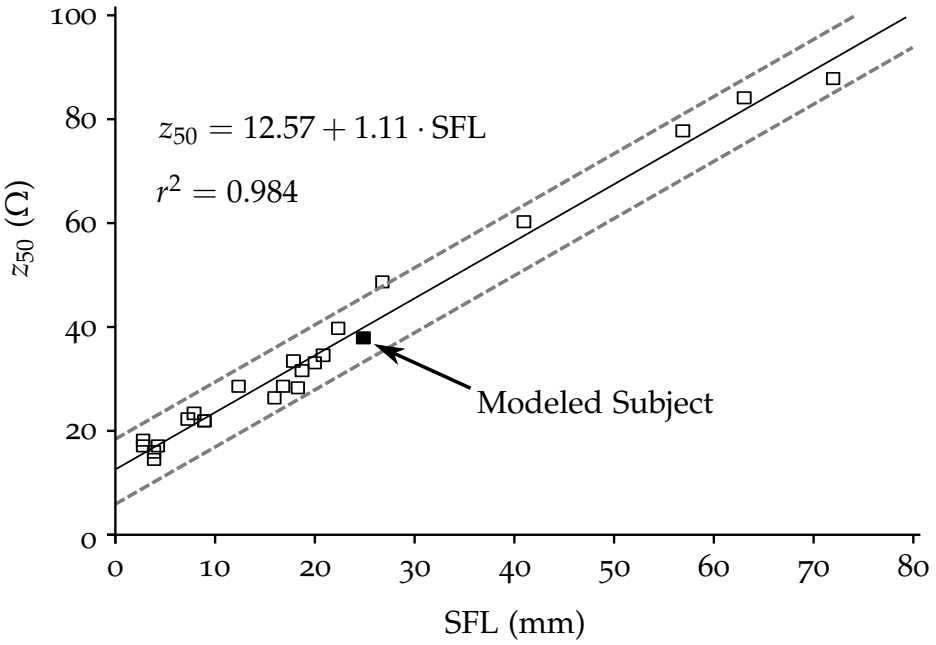

Figure 3.3: Regression line and 95 % prediction intervals for the correlation between SFL and impedance from pooled data at 50 kHz. Modified from Scharfetter et al., 2001.

with 50 Hz, where the slope of the regression line between the SFL and the measured impedance z was reported to be $1.11\,\Omega/\mathrm{mm}$ with a coefficient of determination $r^2 = 0.984$. This linear correlation between z and the SFL is far from intuitively evident. Other publications such as Gonzalez, Zuniga, and Padilla, 1997 report strongly nonlinear relationships, which might be due to a different electrode spacing.

The purpose of this work is to analyze the influence of different abdominal compartments as well as the hydration state on the measured impedance. Furthermore, we aim to quantitatively explain the regression line between the SFL and z as reported in Scharfetter et al., 2001.

We hypothesize that the following structural factors influence the impedance:

- Visceral fat content,
- geometry of the fat layer below the electrodes, and

- abdominal muscle mass and adipose structures embedded in the muscle ("adipose bridges" in Figure 3.2).

To test this hypothesis and to explain the influences on the measured impedance, we derived a mathematical model which relates the quantities of interest (i. e. the fat fractions in the different compartments and the SFL) to the impedance at multiple frequencies. This model also includes interfering quantities like tissue hydration parameters. We compared our results to measured data from Scharfetter et al., 2001 for the modeled subject in Figure 3.3. This subject had a SFL of 25 mm, and the measured impedance was 38.2 Ω.

3.2 Methods

3.2.1 Hierarchical structural model

A suitable model should ideally link the measured impedance data $\mathbf{z}$ to a parameter vector $\mathbf{q}$. Here, $\mathbf{q}$ should represent the parameters of interest, i. e. physiological parameters which are easily interpretable like the fat fractions in different compartments. The mapping from the measured data $\mathbf{z}$ to this parameter vector $\mathbf{q}$ can be written as

$$\mathbf{z} = \Psi\left(\mathbf{q}, \mathrm{SFL}\right), \tag{3.1}$$

where $\mathbf{z}$ is the transimpedance vector between the voltage measuring electrodes at n different frequencies. Therefore, $\mathbf{z}$ is a row vector of dimension $1 \times n$.

This direct link between $\mathbf{z}$ and $\mathbf{q}$ cannot be realized in practice. Therefore, we developed a hierarchical formulation for this mapping instead. This mapping consists of two steps:

First step: Relates the measured data to the electrical conductivity distribution using a macroscopic electrical volume conductor model of the

abdomen (macroscopic model). To reduce the complexity of the problem, we assumed that the different compartments have homogeneous conductivities. This mapping can be written as

$$\mathbf{z} = \Psi\left(\mathbf{p}, \mathrm{SFL}\right), \tag{3.2}$$

where $\mathbf{p}$ consists of the different electrical conductivities of all the compartments included in the model.

Second step: Describes the conductivity of each individual compartment using an electrical tissue model, which relates the microstructural properties $\mathbf{q}$ of the tissue to the frequency-dependent conductivities $\mathbf{p}$. All tissue models together are described by

$$\mathbf{p} = \chi\left(\mathbf{q}\right). \tag{3.3}$$

This equation is subsequently referred to as the microstructural model.

The macroscopic model contains four internal compartments: subcutaneous fat, muscle, mesentery, and spine. The quantities of interest are the fat fraction in the muscle compartment, the fat fraction in the mesentery, the SFL as defined in Figure 3.2, and the indicators for the intra- and extracellular fluid content in the abdominal muscle and the mesenteric compartment. These indicators are included because they are the most important interfering quantities.

When introducing a hierarchy of two modeling layers as shown in Figure 3.4, the complete model can be written as

$$\mathbf{z} = \Psi\left(\chi\left(\mathbf{q}\right), \mathrm{SFL}\right). \tag{3.4}$$

Except for the SFL, all quantities of interest are parameters of the microstructural tissue models used for the different compartments.

The measured data are obtained by measuring the potential distribution Ψ_E on the body surface during application of an excitation current I.

The macroscopic mapping $\Psi\left(\mathbf{p}, \mathrm{SFL}\right)$ is done by solving the elliptic partial differential equation

$$\begin{aligned} \nabla \cdot (\kappa \nabla \Phi) &= 0 \quad \text{in } \Omega, \\ -\kappa \frac{\partial \Phi}{\partial n} &= \mathbf{J} \cdot \mathbf{n} = J_0 \quad \text{on } \partial\Omega. \end{aligned} \tag{3.5}$$

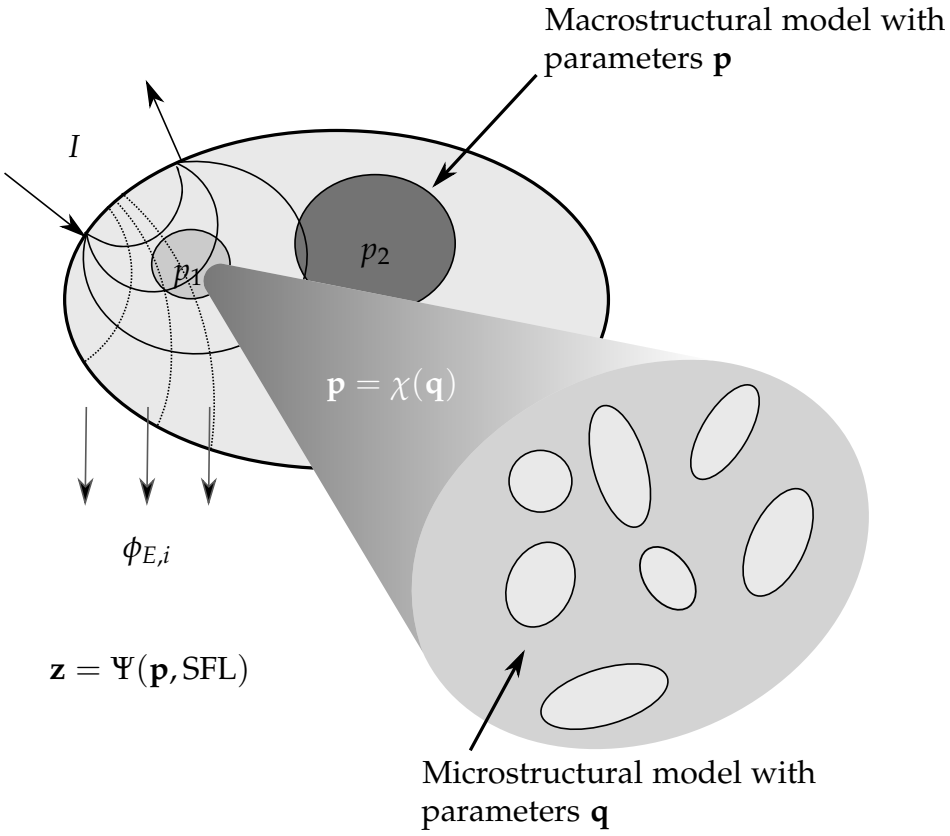

Figure 3.4: Hierarchical model which maps the quantities of interest to the conductivities of the different anatomical compartments. Modified from Scharfetter et al., 2005.

In this equation, J_0 is the normal component of the current density on the boundary, and Φ is the electrical potential. The potential at the outermost distal face of the current injection electrode was prescribed as a Dirichlet boundary condition. The homogeneous Neumann boundary conditions on all remaining surfaces of $\partial\Omega$ were fulfilled automatically by the chosen finite element (FE) approach. The underlying anatomical structure is rather complicated (see Figure 3.2, which shows the transversal cross-section at the height of the umbilicus). The gross structures are electrodes, skin, the SFL, muscles, mesenteric structures (intestine, visceral fat, internal organs) and vertebrae/bone. We applied the finite element method (FEM) for solving the above current field problem.

We neglected the skin in our FE model, because modeling the well conducting but very thin corium (which is about 1–2 mm thick) would have required an enormous number of elements and nodes. Due to its thinness, the corium contributes only marginally to the overall impedance. Therefore, neglecting it is not a problem at all, which was demonstrated using a simple two-dimensional model of two infinitely long coaxial cylinders. A semi-analytic solution for this model was published by (Cheney, Isaacson, and Isaacson, 1990). In short, the electrodes were connected directly to the outermost surface (the subcutaneous fat) in our FE model.

We generated the FE model for subject 7 of the study published in Scharfetter et al., 2001. This subject has a SFL of 25 mm. Fifteen magnetic resonance (MR) images were manually segmented using a custom MATLAB[1]-based program developed by the Institute of Biomedical Engineering. The electrodes were placed according to Figure 3.2 and automatically inserted onto the outer contour of the subcutaneous fat. All node coordinates were extracted and automatically imported into the commercial meshing tool HYPERMESH[2]. Based on these geometries, a non-uniform tetrahedral mesh using second order tetrahedra with ten nodes each was generated in order to smoothly approximate the surfaces. The forward solution was carried out with an existing, in-house solver which employs the incomplete Cholesky conjugate gradient method (Jacobs, 1980; Kershaw, 1978).

Figure 3.5 shows the geometry and discretization of the FE model. This

[1] Natick, MA, USA
[2] Altair Engineering, Troy, Michigan

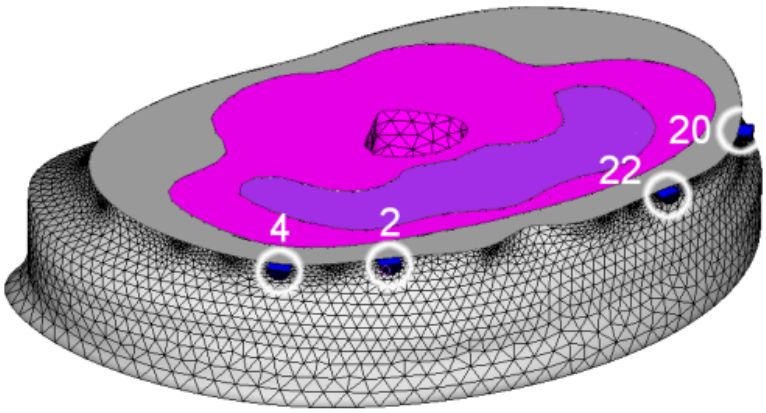

Figure 3.5: FE model with segmentation of different compartments (different colors) and discretization (triangular mesh). Electrodes 4 and 20 were used for current injection, whereas electrodes 2 and 22 were used for voltage measurement. The spacing of the electrodes is equivalent to the measurement setup shown in Figure 3.2. Modified from Scharfetter et al., 2005.

model consists of 24 electrodes, but for the analysis of the problems stated here, only electrodes 4/20 and 2/22 were used as current injection electrodes and voltage measuring electrodes, respectively.

The transimpedances z_i were calculated from the potential on the voltage sensing electrode and the current through the surface of the injection electrode at different frequencies f_i according to

$$\mathbf{z} = \mathrm{col}\,(z_i) = \mathrm{col}\left(\frac{\Phi_i|\partial\Omega_E}{I}\right), \tag{3.6}$$

where $\partial\Omega_E$ denotes the metallic face of the electrode boundary.

3.2.2 Microscopic models

Subcutaneous fat

We modeled the subcutaneous fat (SF) as a homogeneous isotropic conductor. The conductivity spectrum is not very well defined and only few in

vivo data are available (Gabriel, Gabriel, and Corthout, 1996; Gabriel, Lau, and Corthout, 1996; Jossinet, 1998; Jossinet, 1996). Since good microstructural models for the SF are not available, the mean spectrum from Jossinet, 1996 was approximated by a polynomial with four complex parameters ϑ_i and four tuning parameters q_i given in Equation 3.7 (where ω is the angular frequency of the excitation current). The parameter q_4 controls the absolute value of the conductivity without changing the morphology of its spectrum.

$$\kappa_{\mathrm{f}}(\omega) = q_0 \left(\vartheta_0 + \sum_{i=1}^{3} q_i \vartheta_i \left(\log \omega \right)^i \right) \tag{3.7}$$

Abdominal muscles

In reality, abdominal muscles show anisotropic conductivities. For the musculus rectus abdominis, the musculus psoas major, the musculus psoas minor, and the musculus erector spinae, the fiber orientation can be assumed to be parallel to the longitudinal body axis. This assumption certainly does not hold for the musculus transversus abdominis and the musculus obliquus abdominis.

The effective conductivity of the musculus transversus abdominis can be estimated according to the analytical equation for the resistivity of an anisotropic medium published in Rush, Abildskov, and McFee, 1963. If the electrodes are placed in a plane perpendicular to the fiber orientation, $\sqrt{\rho_{\mathrm{tr}} \cdot \rho_{\mathrm{long}}}$ gives the overall resistivity. In this equation, ρ_{tr} is the resistivity of the transversal muscle, and ρ_{long} is the resistivity of the longitudinal muscle.

Published conductivity values for muscular tissues at low frequencies are highly divergent (see e. g. Gabriel, Lau, and Gabriel, 1996; Geddes and Baker, 1967; Gielen, Jonge, and Boon, 1984; McRae and Esrick, 1993). The absolute values range from 0.11 to 0.34 S/m, and the transversal to longitudinal ratios range from 1.8 to 15.3. Calculating the theoretical range for the conductivity at low frequencies for anisotropic muscular tissue thus yields values between 0.15 to 1.32 S/m. Due to this high degree of uncertainty, the microscopic

model for muscular tissue was kept as simple as possible, assuming one single homogeneous and isotropic muscle compartment with a conductivity spectrum described by a Cole model (Rigaud et al., 1994; Rigaud et al., 1995):

$$\kappa_{\mathrm{m}} = \sigma_{\infty,\mathrm{m}} + \frac{\sigma_{0,\mathrm{m}} - \sigma_{\infty,\mathrm{m}}}{1 + \left(j\frac{\omega}{2\pi f_{c,\mathrm{m}}}\right)^{\alpha_{\mathrm{m}}}} \tag{3.8}$$

The Cole parameters $\sigma_{0,\mathrm{m}}$ and $\sigma_{\infty,\mathrm{m}}$ are the conductivities of the muscular compartment at low and high frequencies, respectively. These parameters are indicators for the hydration state of the tissue, where $\sigma_{0,\mathrm{m}}$ is correlated with the extracellular volume (ECV) and $\sigma_{\infty,\mathrm{m}}$ is correlated with both the ECV and the intracellular volume (ICV).

We selected the conductivity values in such a way that the model optimally approximates the measured impedance. The choice of these values is not critical, because these values have a comparatively small influence on the slope $\frac{dz}{d\mathrm{SFL}}$. Table 3.1 lists the values used for the microscopic model.

When inspecting the MRI images used for creating the FE model, it can be observed that the muscle compartment also contains adipose structures which depend on the degree of obesity (see Figure 3.2). These "adipose bridges" increase the impedance of the muscle in the direction of the current flow. This fact was taken into account by using Equation 3.9, which models the effective impeditivity as the weighted sum of the impeditivities of pure muscle and adipose tissue. In this equation, w_{m} is the fat fraction in the muscle compartment.

$$\rho_{\mathrm{ma}}(\omega) = \left[(1 - w_{\mathrm{m}}) \cdot \rho_{\mathrm{m}}(\omega) + w_{\mathrm{m}} \cdot \rho_{\mathrm{f}}(\omega)\right] \tag{3.9}$$

Physically, this model is not correct, because in reality there is a non-linear relationship between the muscular fat fraction and the measured impeditivity (see e. g. Fricke, 1924). However, since the exact geometry of the fatty substructures is not clearly defined, it is impossible to formulate a valid mathematical description. Therefore, a very simple linear superposition model is chosen.

For complex conductivities, which are the reciprocals of impeditivities, Equation 3.9 can be written as

$$\kappa_{\mathrm{ma}} = \left[(1 - w_{\mathrm{m}}) \cdot \kappa_{\mathrm{m}}^{-1} + w_{\mathrm{m}} \cdot \kappa_{\mathrm{f}}^{-1}\right]^{-1}, \tag{3.10}$$

Table 3.1: Microscopic parameter vector $\mathbf{q}$.

	Variable	Description	Value
q_1	q_1	First coefficient of fat polynomial	$7.3447 \cdot 10^{-4}$
q_2	q_2	Second coefficient of fat polynomial	-0.0121
q_3	q_3	Third coefficient of fat polynomial	0.0685
q_4	q_0	Scaling factor of fat polynomial	-0.0679
q_5	$\sigma_{0,\mathrm{m}}$	σ_0 of the muscular Cole model	0.25 S/m
q_6	$\sigma_{\infty,\mathrm{m}}$	σ_∞ of the muscular Cole model	0.6 S/m
q_7	$f_{c,\mathrm{m}}$	Characteristic frequency of the muscle	273 kHz
q_8	α_m	Cole exponent of the muscle tissue	0.8
q_9	$\sigma_{0,\mathrm{l}}$	σ_0 of the mesenteric Cole model	0.5 S/m
q_{10}	$\sigma_{\infty,\mathrm{l}}$	σ_∞ of the mesenteric Cole model	1 S/m
q_{11}	$f_{c,\mathrm{l}}$	Characteristic frequency of the mesentery	2700 kHz
q_{12}	α_l	Cole exponent of the mesenteric tissue	0.5
q_{13}	w_m	Fat fraction in the muscle compartment	0.01
q_{14}	w_a	Visceral fat fraction	0.6
q_{15}	SFL	Thickness of the subcutaneous fat layer	$25 \cdot 10^{-3}$ m

where κ_m is the complex conductivity of the pure muscle tissue (defined using a Cole model like the one stated in Equation 3.8), and κ_f is the complex conductivity of the adipose tissue (see Equation 3.7).

Mesenteric compartment

The real geometry of the mesentery is very complex and the location of fine internal structures remains uncertain due to peristaltic movements. Furthermore, impedance methods are known to have a poor sensitivity for structures far away from the electrode positions. Therefore, we decided to model the mesentery as a single homogeneous conductor, which is enclosed by the muscle compartment and the SF compartment.

Similar to previously employed hydration models (Hanai, 1960), we assumed the visceral fat to be suspended in the form of small adipose spheres in a surrounding medium (which represents the colon and other lean structures from the mesenterium). This surrounding medium exhibits a dispersion described by a Cole model. The conductivity κ_a of such a suspension is modeled by a Fricke model (Fricke, 1924) described in Equation 3.11. Here, β_F is a shape factor for spherical particles, and w_a is the fat fraction in the mesenteric compartment.

$$\begin{aligned} \left(\frac{\kappa_a - \kappa_l}{\kappa_f - \kappa_a}\right) \cdot \left(\frac{\kappa_f}{\kappa_l} - 1\right) &= \frac{\beta_F \cdot w_a}{1 - w_a} \\ \beta_F &= \frac{3\,(\kappa_f - \kappa_l)}{2\kappa_l + \kappa_f} \end{aligned} \tag{3.11}$$

The conductivity of the fat globules κ_f is again described using Equation 3.7, and the conductivity of the lean surrounding medium is described by a Cole model:

$$\kappa_l = \sigma_{\infty,l} + \frac{\sigma_{0,l} - \sigma_{\infty,l}}{1 + \left(j\frac{\omega}{2\pi f_{c,l}}\right)^{\alpha_l}}. \tag{3.12}$$

According to Rigaud et al., 1994, the specific impedance κ_l^{-1} of intestine exhibits two superimposed dispersions, one with a very low characteristic frequency of 520 Hz, and a second one with a high characteristic frequency of about 2.7 MHz. The measurement data from Scharfetter et al., 2001 are only given for frequencies ≥ 5 kHz. Thus, only the second dispersion was considered. Table 3.1 lists the corresponding Cole parameters $\sigma_{0,m}$, $\sigma_{\infty,m}$, $f_{c,m}$, and α_m.

Spine and bones

The conductivities of the vertebrae and bones are very low (significantly lower than 0.05 S/m at frequencies < 500 kHz, see Geddes and Baker, 1967). Therefore, these structures were modeled as insulators.

Electrodes

Each electrode was modeled as a cylinder representing the electrode gel. The diameter of a cylinder was 1 cm, the conductivity was 10 S/m, and the relative permittivity was set to 80, all of which are typical values for ECG electrodes. The base surface was fitted to the irregular body surface to realistically simulate the tight fit. The distal face of the cylinder ($\partial\Omega_{E,i}$ in Equation 3.6) was assumed as an equipotential surface with a potential of 10 V. The current was calculated by integrating the gradient of the potential over the contact surface between the gel layer and the subcutaneous fat compartment.

The macroscopic parameter vector can now be written as the conductivities of the following three different compartments: the SF, the muscle, and the mesenterium:

$$\mathbf{p} = [\kappa_f, \kappa_{ma}, \kappa_a] .$$

The microscopic parameter vector consists of all the parameters of interest (except for the geometric parameter SFL) which were included in the microstructural tissue models:

$$\mathbf{q} = [\vartheta_1 \dots \vartheta_4, \sigma_{0,m}, \sigma_{\infty,m}, f_m, \alpha_m, \sigma_{0,l}, \sigma_{\infty,l}, f_l, \alpha_l, w_m, w_a] .$$

3.2.3 Sensitivity analysis

To answer questions like how much the different abdominal compartments or the hydration state contribute to the overall measured impedance, it is necessary to calculate the differential sensitivity of $\mathbf{z}$ with respect to all the parameters $\mathbf{q}$ and the geometrical parameter SFL. These calculations are summarized in the sensitivity matrix

$$\mathbf{G} = \left[\frac{d\Psi}{d\mathbf{q}}, \frac{d\Psi}{d\mathrm{SFL}} \right] . \tag{3.13}$$

The calculation of $\Psi(\mathbf{q}, \mathrm{SFL})$ entails computing the solution of a FE problem. Therefore, the direct differentiation of Ψ with respect to the fifteen

parameters would be computationally expensive. Fortunately, this effort can be reduced because of the hierarchical model structure $\Psi(\mathbf{q}, \mathrm{SFL}) = \Psi(\chi(\mathbf{q}), \mathrm{SFL})$ by applying the chain rule to Equation 3.13:

$$\mathbf{G} = \left[\frac{\partial \Psi}{\partial \mathbf{p}} \cdot \frac{\partial \chi}{\partial \mathbf{q}}, \ \frac{d\Psi}{d\mathrm{SFL}} \right] \tag{3.14}$$

Thus, the function Ψ only needs to be differentiated with respect to the three components of $\mathbf{p}$ (the three different conductivities in the three compartments) and the SFL. The differentiation of the microscopic models χ with respect to $\mathbf{q}$ can be carried out efficiently using the symbolic toolbox of MATLAB. Since the model is non-linear in the parameters, the sensitivity matrix depends on the actual values of the parameter vector $\mathbf{q}$. Therefore, the crucial point is the adequate choice of the model parameters, many of which are not known with high accuracy. Some parameters (like the Cole parameters for muscle tissue or the Cole parameters for the fat spectra) can be obtained from the literature, but for example the fat fractions are in general unknown. These parameter values were chosen in such a way that both the simulated impedance as well as the slope of the regression line $\frac{dz}{d\mathrm{SFL}}$ approximate the experimental data in Scharfetter et al., 2001 to a maximum extent.

To obtain changes of the impedance z_i per percent change of the parameter q_k ($\Omega/\%$) which are straightforward to analyze, the sensitivity vector $\mathbf{G}$ was normalized. Only for the SFL, the unnormalized sensitivity Ω/m was used:

$$\bar{g}_{ik} = \left[0.01 \frac{dz_i}{dq_k/q_k}, \ \frac{dz_i}{d\mathrm{SFL}} \right]. \tag{3.15}$$

Since it is not possible to compute the sensitivity for the SFL analytically, this value was computed using a differential inflation of the outermost boundary of the FE model, thereby reducing the SFL marginally. Therefore,

every node of the surface was moved along its outward normal vector

$$\begin{aligned} \frac{dz_i}{d\mathrm{SFL}} &= \sum_l \frac{dz_i}{d\mathbf{x}_l} \frac{d\mathbf{x}_l}{d\mathrm{SFL}}, \\ \frac{d\mathbf{x}_l}{d\mathrm{SFL}} &= \lim_{\delta \to 0} \frac{\mathbf{x}_l + \delta \mathbf{n}_l - \mathbf{x}_l}{\delta} = \mathbf{n}_l. \end{aligned} \tag{3.16}$$

Here, dSFL denotes the differential shift of the nodes of the shifted surface, $\mathbf{n}_l$ is the unit outward normal vector in the node l with the coordinate vector $\mathbf{x}_l$. The differential quotient was calculated numerically by using finite differences. The partial derivative of the coordinate vector with respect to dSFL is equal to $\mathbf{n}_l$.

3.3 Results

The calculated impedance for the simulated subject was close to the one measured in Scharfetter et al., 2001 (37.2 Ω simulated as opposed to 38.2 Ω measured).

The sensitivity for the SFL was calculated with 0.52 Ω/mm. Expressed as a percentage, this means a contribution of about 47 % of the SFL's sensitivity to the total slope of the experimental regression line (which was about 1.1 Ω/mm).

The normalized sensitivity of the impedance with respect to the muscular fat content was calculated to be 0.006 Ω per percent change of w_m. The sensitivity to the mesenteric fat was calculated to be 0.174 Ω per percent change of w_a and is thus significantly higher.

The sensitivity to the muscular Cole parameter $\sigma_{0,\mathrm{m}}$ (q_5) is quite high at low frequencies, namely 0.104 Ω per percent change at 50 kHz. On the other hand, the sensitivity of $\sigma_{\infty,\mathrm{m}}$ (q_6) is low at low frequencies, the calculated value was 0.058 Ω per percent change.

3.4 Discussion

The presented structural model in combination with the proposed sensitivity analysis is the most comprehensive approach for the investigation of body composition measurements using BIA. Nevertheless, this model has not been validated yet, although it helps to gain further insight into and might help to improve BIA methods.

With the model introduced in this chapter, only about 42 % of the experimentally observed regression line slope can be attributed to the SFL. The remaining 58 % may be explained by a change of the mesenteric and the muscular fat content.

An increase of the SFL by 1 mm yields an increase of the impedance by about 0.52 Ω. Using the modeled SFL of 25 mm, this corresponds to a four percent change. Assuming a strict one-to-one coupling of the percent changes in all three fat fractions and thus proposing this 4 % change to both the muscular and the mesenteric fat content would yield a change in the impedance of about 0.024 Ω and 0.696 Ω, respectively. Summing up these three impedance gains yields an increase of 1.2 Ω, which is very close to the experimentally observed value of 1.1 Ω. The fat content of the visceral compartments is therefore clearly reflected in the measured impedance.

This result, although highly promising, only holds if all the other parameters remain constant. However, the sensitivity analysis also showed a high sensitivity of the measured impedance to the electrical properties of the muscular compartment (0.104 Ω change per percent change of $\sigma_{0,m}$). Assuming a linear relationship between the muscular ECV and $\sigma_{0,m}$ thus means that an increase of the ECV by 4 % would produce an impedance change of about 0.5 Ω and thus mimicking a decrease of the SFL by about 0.5 mm. A separation of these effects is not possible with the tetrapolar arrangement chosen in this work. Therefore, one has to bare in mind that it is only possible to monitor the fat content if the subject has a constant hydration state and if the ratio between muscle mass and SFL corresponds to a “normal” collective.

The model also suffers from the usual modeling restrictions since it incorporates great simplifications when compared to the complex human

anatomical and physiological system. Important limitations are:

- The FE model includes the anatomical structures up to 8 cm below and above the electrode plane. Any currents which in reality may flow outside of this modeled volume are neglected. However, as these currents do not contribute more than 10 % to the overall current, the resulting error should be negligible.
- Any dynamic changes in the model like respiratory movements or the filling state of the bladder were neglected. However, because the subjects from the published measurements in Scharfetter et al., 2001 held their breath during the measurements, the respiratory effects were eliminated. The filling state of the bladder should be randomly distributed among all subjects and thus should not significantly affect the mean slope of the regression line $\frac{dz}{d\mathrm{SFL}}$ for a large number of subjects.
- The microscopic tissue models contain physically invalid assumptions. Especially the modeling of the impeditivity of the muscle compartment as a serial connection of the impeditivities of pure muscle tissue and of adipose tissue may be criticized. However, more complex tissue models would increase the uncertainty of the reconstructed parameters and thus the suggested approach is a good compromise.
- Although the applied model appears to explain the slope of the experimental regression line, it should be kept in mind that both the body shape and the real fat distribution affect the sensitivity significantly. Therefore, this analysis is only valid for values of SFL around 25 mm because this is the SFL value of the modeled subject. It would be interesting to find out whether the sensitivity to the mesenteric adipose tissue is also different at different SFLs. This question could be investigated first qualitatively by simple two- or three-layer models (see Elia and Ward, 1999; Robinson and Coruh, 1988) and in a second step quantitatively by anatomically more realistic models.
- The implemented sensitivity analysis provides only local sensitivity information, because the calculated sensitivity values depend on the exact value of the parameters. The calculated sensitivities are therefore only valid for parameter values which do not differ too much from the ones used in this work.

3.5 Conclusion

The results clearly show that impedance measurements for the chosen electrode configuration is sensitive not only to the SFL but also to the fat content in deep structures such as the mesentery.

Hierarchical structural models like the one developed in this work provide a valuable tool for the a-priori assessment of BIA. For the problem stated above, the hierarchical structural model helped to achieve a better understanding of the experimental results and clarify the origin of the slope of the regression line between the SFL and the measured impedances. This understanding is a prerequisite for a sound data interpretation.

Future work should concentrate on the following problems. First, the influence of changes in the geometry of the FE models on the parameters should be investigated. Second, a collection of FE models for subjects with different SFLs should be created and compared with simple two- or three-layer models. Finally, fitting algorithms for the reconstruction of the parameters using multi-electrode and multi-frequency measurements should be implemented.

4 Optimization approach for illuminating highly scattering tissue

4.1 Introduction

The use of optical imaging (OI) is of special interest in biological and medical sciences. Diagnostic and therapeutic instruments which are based on visible, near-infrared, or near-ultraviolet light have many advantages as compared to e. g. MRI. The equipment is affordable, and data acquisition is usually fast. However, some inherent problems still remain to be solved. These problems are mainly due to the highly scattering nature of biological tissue in the frequency spectrum used in optical tomography (OT). High scattering coefficients cause the photons to propagate non-deterministically. Therefore, the measurement of superficial structures as well as a selective illumination of deeper regions are complicated tasks. As a result, the determination of the optimal placement of optodes is not trivial except for simple regular geometries like cylinders or spheres.

Several numerical methods for the optimization of the hardware setup in strongly scattering tissues were developed recently. Culver et al., 2001 used a singular value analysis (SVA) of the sensitivity matrix to compare measurement setups with different optode spacings or different measurement types (reflectance vs. transmittance setup). Xu et al., 2003 compared two different optode configurations for a hydrid MRI/DOT system, using the number of singular values above a certain threshold as a quality criterion. Graves et al., 2004 also used SVA for the evaluation of several 2D fluorescence

tomography setups, and Lasser and Ntziachristos, 2007 applied the same procedure for 3D setups.

A similar problem of determining the optimal locations and magnitudes for all optodes occurs in PDT (see e. g. Dolmans, Fukumura, and Jain, 2003). PDT is used for oncological treatments (e. g. for esophageal cancers, especially at a stage where surgical intervention is not indicated), as well as for dermatological treatments (e. g. for the treatment of actinic keratosis, acne vulgaris or granuloma annulare, among others, see e. g. Babilas and Szeimies, 2010). It appears attractive to extend PDT to other carcinomas on epi- or endothelial surfaces, and clinical trials are carried out for example for cervix carcinomas.

Other potential candidates, mesotheliomas of the thoracic cavity, represent a special challenge. They are difficult to treat and the design of an appropriate light applicator is especially difficult. In contrast to applications with simple geometries like the esophageal cavity, the geometry of the intrathoracic cavity is very complex. Therefore, standard cylindrical scattering devices which are used in the esophageal cavity are not suitable due to their small and curved area of treatment. Using these standard devices for the illumination of the intrathoracic cavity would lead to significant inhomogeneities. These can lead to locally ineffective treatment or, even more seriously, to lethal overdoses (Schouwink and Baas, 2004).

In the past, several designs for flexible light diffusers have been proposed. A typical solution is to use cylindrical or spherical diffusers in a bag filled with a scattering medium. Although these light diffusers are applicable after pneumonectomia, they have to be rinsed continuously to prevent blood accumulations at the surface of the bags (Dwyer et al., 2000; Friedberg et al., 2003; Krueger et al., 2003; Baas et al., 1997). Some regions like the sinus diaphragmaticus are difficult to access and have to be illuminated separately. This can be achieved with wedge-shaped illuminators (van Veen et al., 2001). However, the positioning of these illuminators and achieving a homogeneous illumination using these illuminators is challenging. Another approach is to fill the thorax with a biologically non-hazardous scattering medium (e. g. with intralipid), which can simultaneously be used for rinsing to avoid blood accumulation. Typically, a spherical diffuser is used for illumination, but controlling the dose rate is difficult using this approach.

This method has also been applied to cases where lung tissue was not resected (Friedberg et al., 2003).

In general, both methods try to achieve homogeneous fluence using real-time dosimetry and manual repositioning of the light diffuser. An interesting alternative is the use of textile-based diffusers with integrated optical fibers. These diffusers are extremely flexible but suffer from inhomogeneous illumination and a low transmission rate Selm et al., 2007; Rothmaier et al., 2008. Recently, so-called "light blankets" with arrays of cylindrical diffusers Hu, Wang, and Zhu, 2009, as well as a spirally-wound side-glowing fibers Hu, Wang, and Zhu, 2010 embedded in a bag filled with intralipid were presented. They are easy to fabricate, but still show inhomogeneities, especially at the corners. Due to the need for a homogeneous fluence rate, it is of great interest to optimize the placement of these fibers, which results in improved illumination using minimal energy.

The purpose of this work is to implement a general approach for the determination of adapted optode locations for different geometries, tissue types, and applications. The method is based on considering this task as an optimal control problem for a partial differential equation describing the diffusion of photons in a strongly scattering medium, where the locations of optodes are modeled as a continuous "source field". The crucial step is to include a penalty term that favors point-wise solutions. This approach was first published in Stadler, 2009. That way, the locations as well as the magnitudes of the light sources are obtained in a single step. The main advantages of this approach over previously published discrete methods are that no initial maximal or minimal configuration needs to be specified (although an allowable region can be enforced), and that a combinatorial problem with exponential complexity is avoided. In addition, the algorithm is not based on stochastic methods (like e. g. Monte Carlo methods), but is fully deterministic, which facilitates the verification of the outcome significantly. Finally, the approach is flexible and can incorporate a wide variety of objective criteria (e. g. photon flux over a given boundary section) by changing the target functional. The proposed approach is demonstrated in the context of optimizing the illumination pattern for the PDT of intrathoracic cancer.

4.2 Theory

During PDT, a photosensitizer, for example Photofrin, is injected intravenously. Afterwards, the cancerous tissue is illuminated using red to near-infrared light from diffuse sources. The light is directly applied to the region of interest, in the case of intrathoric cancer to the intrathoracic cavity. The absorption of energy by the photodynamic drug leads to the formation of cytotoxic singlet oxygen and hydroxyl radicals, which destroy cancer cells selectively (see Section 2.2.2). The challenge is to homogenize the light intensity as both under- and overexposure can lead to ineffective treatment (Henderson et al., 2000).

4.2.1 Mathematical model

The diffusion approximation of the RTE was used for modeling the steady state of light propagation in scattering medium (Arridge, 1999). This leads to a stationary elliptic partial differential equation which describes the photon distribution $\varphi \in H^1(\Omega)$

$$\begin{cases} -\nabla \cdot (\kappa(x)\nabla\varphi(x)) + \mu_a(x)\varphi(x) = q(x) & \text{in } \Omega, \\ \qquad \kappa(x)\,\vec{n}(x) \cdot \nabla\varphi(x) + \rho\varphi(x) = 0 & \text{on } \Gamma. \end{cases} \tag{4.1}$$

The geometry of the object is given by the domain $\Omega \subset \mathbb{R}^d$, $d \in \{2, 3\}$ being the number of spatial dimensions, with boundary Γ whose outward normal vector is denoted by $\vec{n}$. The medium is characterized by the absorption coefficient μ_a, the reduced scattering coefficient μ_s', and the diffusion coefficient $\kappa = \left[\frac{1}{d}(\mu_a + \mu_s')\right]^{-1}$. The coefficient ρ models the reflection of a part of the photons at the boundary due to a mismatch in the index of refraction. Finally, the source term q models the light emission of the embedded optodes (see also Section 2.2.5).

For the optimal control approach, the solution $p \in H^1(\Omega)$ of the adjoint equation is also required:

$$\begin{cases} -\nabla \cdot (\kappa(x)\nabla p(x)) + \mu_a(x)p(x) = f(x) & \text{in } \Omega, \\ \qquad \kappa(x)\,\vec{n}(x) \cdot \nabla p(x) + \rho p(x) = 0 & \text{on } \Gamma \end{cases} \tag{4.2}$$

for given $f \in L^2(\Omega)$. Both equations should be understood in the weak sense.

4.2.2 Optode placement optimization

Since optodes act as discrete light sources, the source term can be modeled as

$$q(x) = \sum_{j=1}^{N} q_j \delta(x - x_j) \quad \text{for } q_j \in \mathbb{R}_+,\ x_j \in \Omega,\ 1 \leq j \leq N, \tag{4.3}$$

where δ denotes the Dirac distribution with $\int f(x)\, \delta\{dx\} = f(0)$ for all continuous functions f.

A straightforward approach for optimizing the placement of the optodes would identify a set of $M \gg N$ possible optode locations $x_1, \ldots, x_M$ and chose the best N locations such that a certain performance criterion $J(q)$ is minimized. The corresponding optimal source magnitudes q_j would then be computed in a second step. This was, for example, done in Freiberger, Clason, and Scharfetter, 2010.

To avoid the combinatorial complexity of this discrete approach, instead of specifying the optode locations beforehand, the (distributed) source term q was optimized directly. A penalty term that promotes sparsity of q, i. e. smallness of its support $\{x \in \Omega : q(x) \neq 0\}$, was added. This also has the advantage that the number N of optodes does not need to be specified in advance. For the problem of PDT, point sources are needed. Thus, the source term q was searched for in the space of regular Borel measures (which includes the Dirac distribution). Following Clason and Kunisch, 2011, the optimization problem to be solved can be written as:

$$\min_{q \in \mathcal{M}(\Omega)} J(q) + \alpha \|q\|_{\mathcal{M}}, \tag{4.4}$$

where $\mathcal{M}(\Omega)$ is the space of regular Borel measures, i. e. the dual of the space $C_0(\Omega)$ of continuous functions with compact support on Ω, with norm

$$\|q\|_{\mathcal{M}} = \sup_{\substack{f \in C_0(\Omega) \\ \|f\|_C \leq 1}} \int_\Omega f \, dq, \tag{4.5}$$

which reduces to

$$\|q\|_{\mathcal{M}} = \int_{\Omega} |q(x)|\, dx = \|q\|_{L^1} \tag{4.6}$$

for $q \in L^1(\Omega)$. This is related to the well-known fact that L^1 norms promote sparsity in optimization. The penalty parameter α controls the sparsity of the solution: the larger α, the smaller the support of q.

For PDT, where a homogeneous illumination should be achieved, the performance criterion can be formulated as the deviation from a constant illumination z in an observation region $\omega_o \subset \Omega$ such that $J(q) := \frac{1}{2}\|\varphi|_{\omega_o} - z\|^2_{L^2(\omega_o)}$, where $\varphi|_{\omega_o}$ denotes the restriction of φ to ω_o.

Due to the linearity of the forward problem, it is possible to choose $z = 1\,(\mathrm{Wm}^{-2})$ without loss of generality. After optimization, the magnitude of the resultant sources can be linearly scaled to achieve the required illumination z. In addition, the possible light source locations were restricted to a control region $\omega_q \subset \Omega$, which does not overlap with the observation region ω_o (i. e., $\bar{\omega}_q \cap \bar{\omega}_o = \emptyset$). A non-negative source term q (which represents the optodes) was also enforced.

This leads to the following optimization problem:

$$\min_{\varphi \in H^1(\Omega), q \in \mathcal{M}(\omega_q)} \frac{1}{2}\|\varphi|_{\omega_o} - z\|^2_{L^2(\omega_o)} + \alpha\|q\|_{\mathcal{M}(\omega_q)} \quad \text{subject to (4.1) and } q \geq 0. \tag{4.7}$$

It was shown in Clason and Kunisch, 2012 that this problem has a solution $q^* \in \mathcal{M}(\omega_q)$, which can be approximated by a sequence of functions $q_\gamma \in L^2(\omega_q)$ for $\gamma \to \infty$ satisfying

$$q_\gamma + \gamma \min(0, p_\gamma + \alpha) = 0, \tag{4.8}$$

where p_γ is the solution of (4.2) with right hand side $f := \varphi_\gamma - z$ and φ_γ is the solution of (4.1) with right hand side q_γ. Equation 4.8 can be solved using a semismooth Newton method which is superlinearly convergent (see Clason and Kunisch, 2012). To globalize the Newton method and closely approximate the solution q^* of (4.7), we use a continuation scheme in γ where we iteratively solve the problem for an increasing sequence γ_n using the previous solution as initial guess.

4.2.3 Finite element discretization

The discretization needs to account for the fact that the functions q_γ converge to measures as γ increases. We therefore employ the finite element discretization proposed in Casas, Clason, and Kunisch, 2012, where the photon density φ_γ and the adjoint variable p_γ are discretized using piecewise linear elements on a given triangulation T, while the source term q_γ is discretized using linear combinations of Dirac distributions centered at the interior nodes x_i, $1 \le i \le N(T)$, of T:

$$q_\gamma = \sum_{i=1}^{N(T)} q_i \delta(x - x_i). \tag{4.9}$$

In practice, the number of nodes $N(T)$ will be determined by the need to resolve the geometry of the domain and the required accuracy of the solution of the forward model (4.1). Although further refinement of the triangulation increases the number of possible optode locations, the sparsity-promoting property of the minimized functional discourages placing additional optodes. In fact, it was shown in Casas, Clason, and Kunisch, 2012 that for a given discretization of the forward model, the computed sources (for $\gamma \to \infty$) are optimal among all (non-discretized) measures.

Since the linear finite element basis functions form a nodal basis, the right hand side in the weak formulation of (4.1) for a piecewise linear basis function e_j becomes

$$\langle q_\gamma, e_j \rangle = \sum_{i=1}^{N(T)} q_i \langle \delta(x - x_i), e_j \rangle = q_j, \tag{4.10}$$

i. e. the mass matrix is the identity. Introducing the stiffness matrix A corresponding to (4.1) and the observation mass matrix M_o with entries $M_{ij} = \int_{\omega_o} e_i e_j \, dx$, we obtain the discrete optimality system

$$\begin{cases} A\varphi_\gamma - q_\gamma = 0, \\ -M_o \varphi_\gamma + A^T p_\gamma = -M_o z, \\ q_\gamma + \gamma \min(0, p_\gamma|_{\omega_q} + \alpha) = 0. \end{cases} \tag{4.11}$$

Eliminating q_γ using the last equation and applying a semismooth Newton method (Clason and Kunisch, 2012), we have to solve for (φ^{k+1}, p^{k+1}) the block system

$$\begin{pmatrix} A & D_k \\ -M_o & A \end{pmatrix} \begin{pmatrix} \varphi^{k+1} \\ p^{k+1} \end{pmatrix} = \begin{pmatrix} -\alpha d^k \\ -M_o z \end{pmatrix}, \tag{4.12}$$

where D_k is a diagonal matrix with the entries of the vector d^k,

$$d_j^k = \begin{cases} \gamma & \text{if } (p^k|_{\omega_q})_j < -\alpha, \\ 0 & \text{else,} \end{cases} \tag{4.13}$$

on the diagonal. It can be shown that the semismooth Newton method has converged once $d^{k+1} = d^k$ holds. After the final p^k has been computed, the corresponding control can be obtained from (4.8). The complete procedure is given in Algorithm 1.

Algorithm 1 Semismooth Newton method with continuation.

for $m = 1, \ldots, m^*$ **do**
  set $\gamma = 2^{(m-1)}$, $\varphi^0 = p^0 = d^0 = 0$
  for $k = 0, \ldots, k^*$ **do**
    solve (4.12) for φ^{k+1}, p^{k+1}
    compute d^{k+1} from (4.13)
    if $d^{k+1} = d^k$ **then**
      set $q^{(m)} = \gamma \min(0, p^{k+1}|_{\omega_q} + \alpha)$
      break
    end if
  end for
end for

4.3 Methods

The optimization algorithm described in section 4.2.2 is implemented in Python using the open source finite element library FEniCS (Logg, Mardal, and Wells, 2012). The parameters in Algorithm 1 are set to $m^* = 34$ (such

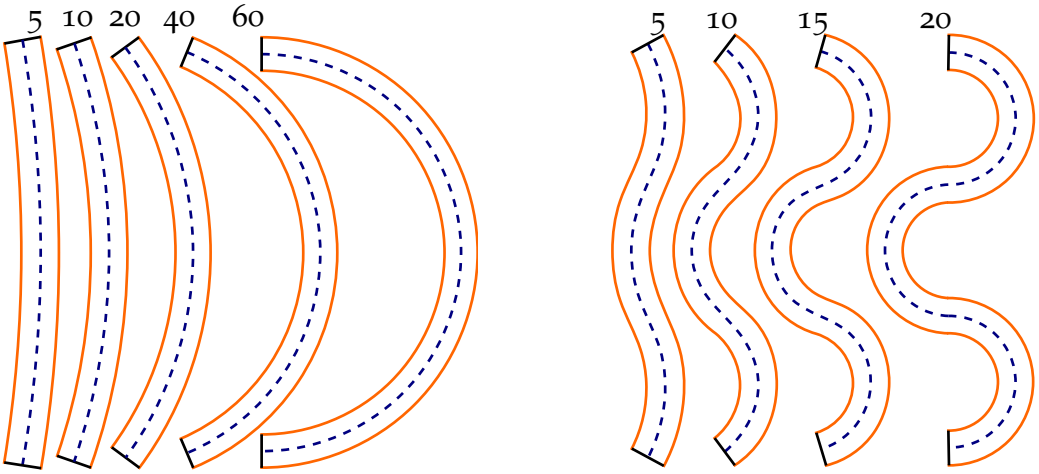

(a) Single-curved models. (b) Double-curved models.

Figure 4.1: Various two-dimensional model geometries (numbers indicate the different curvature κ). From Brunner et al., 2012.

that $\gamma^* \approx 10^{10}$) and $k^* = 20$. To model a textile-based diffuser, the material parameters in (4.1) are taken as $\mu_a = 10^{-4}\,\mathrm{mm}^{-1}$, $\mu_s' = 10^{-1}\,\mathrm{mm}^{-1}$, and $\rho = 0.1992$. The influence of the parameter α is illustrated by comparing the results for different values of α, which are specified below.

The meshes for the light diffusers containing the optodes are created with the commercial mesh generator HYPERMESH. To demonstrate the behavior of the optimization algorithm for different geometries, we first consider simple two-dimensional spline models which represent the cross-section of an infinitely long pad. This geometry mimics that of an array of parallel cylindrical diffusers embedded in a scattering substrate. Five single-curved models and four double-curved models with increasing curvature κ were created as shown in Figure 4.1. The single-curved models mimick the anatomical situation which occurs at intrathoracic PDT. The double-curved models were chosen to show the applicability of the proposed method in situations where intuitive optode placement is not possible anymore. The dimensions correspond approximately to a width of 10 mm and a height of 120 mm.

In all cases, the region ω_o in which the illumination should be homogenized

are the left and right outer lines (indicated in orange in Figure 4.1). The region ω_q (where the optodes are allowed to be placed) is a single line equidistant from both outer lines (indicated by a dashed line in Figure 4.1). The meshes for the single-curved models of curvature $\kappa = 5$, 10, 20, 40, and 60 consist of 61038, 61789, 67160, 80664, and 105322 finite elements, respectively. The curvatures correspond to the transverse reflection of the pad's center in millimeters, with a reflection of 60 mm forming a perfect semicircle as the pad's height is 120 mm. The double-curved models of curvature $\kappa = 5$, 10, 15, and 20 are composed of 62349, 70735, 82119, and 104220 finite elements, respectively.

The photodynamic treatment is simulated by embedding the light diffuser model in the intrapleural space of a realistic three-dimensional human thorax model that is constructed from a stack of CT images. The approximate dimensions of this pad are: height 100 mm, width 150 mm, thickness 10 mm. The observation region ω_o is defined as the outer and inner surface of the model, and ω_q is an interior manifold equidistant from both (see Figure 4.2; ω_q is indicated in purple). The generated mesh consists of 81770 elements.

The results are evaluated quantitatively for different values of the sparsity-controlling parameter α. The coefficient of variation c_v of the resulting photon density φ_γ over the observation region ω_o, as well as the number N of sources after the optimization procedure serve as quality measures. For the latter, all the nodes in the control region ω_q which have a value of $q_\gamma > 10^{-16}$ are counted. We compare the results for $\alpha \in \{0.1, 0.01, 0.001\}$ for the two-dimensional models and $\alpha \in \{0.2, 0.4, \ldots, 1.8\}$ for the three-dimensional model.

4.4 Results

The quantitative results for the two-dimensional geometries are given in Table 4.1 for the single-curved models and in Table 4.2 for the double-curved models, respectively. As can be seen by comparing the number of active nodes N with the total number of nodes for each model, the algorithm indeed produces discrete sources that can be used as optode positions. The

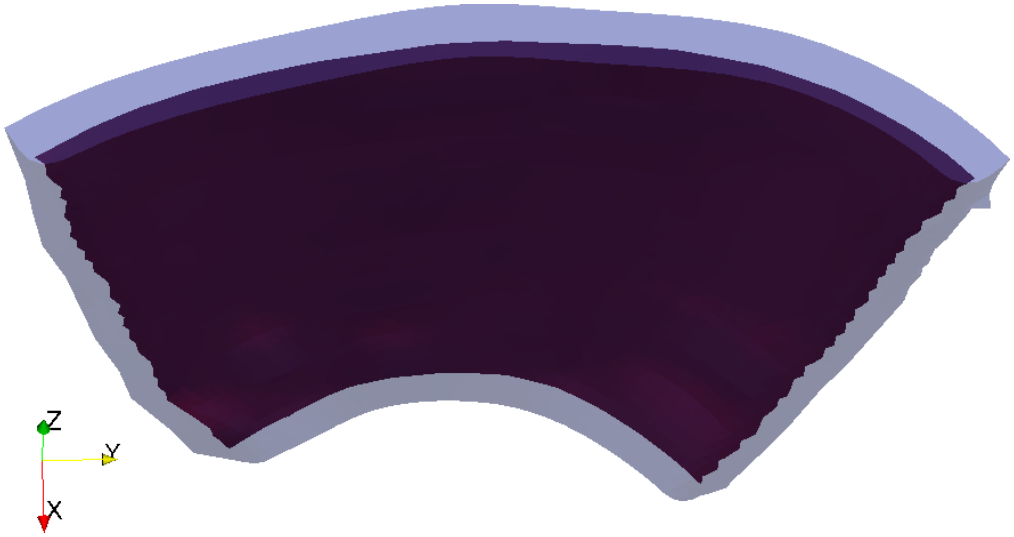

(a) Top oblique view

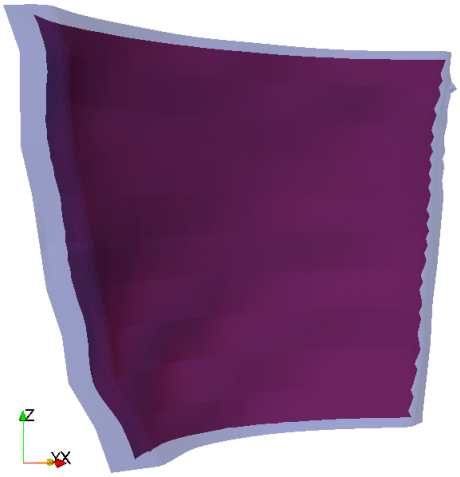

(b) Front oblique view

(c) Side oblique view

Figure 4.2: Three-dimensional model. The admissible manifold ω_q for the optodes is indicated in purple. From Brunner et al., 2012.

Table 4.1: Results for single-curved models. Shown are the number N of active nodes and the coefficient of variation c_v of the photon density in the observation domain for different curvatures κ and values of α.

κ	5			10			20			40			60		
α	0.1	0.01	0.001	0.1	0.01	0.001	0.1	0.01	0.001	0.1	0.01	0.001	0.1	0.01	0.001
N	22	49	59	18	51	83	15	56	66	20	51	62	22	68	147
c_v	0.252	0.0182	0.00540	0.296	0.0207	0.00617	0.178	0.0196	0.00795	0.168	0.0253	0.0109	0.121	0.0202	0.0157

Table 4.2: Results for double-curved models. N indicates the number of active nodes, c_v the coefficient of variation obtained for the photon density in the observation domain for different combinations of curvature κ and penalty parameters α.

κ	5			10			15			20		
α	0.1	0.01	0.001	0.1	0.01	0.001	0.1	0.01	0.001	0.1	0.01	0.001
N	12	50	134	19	40	148	26	49	60	33	77	130
c_v	0.165	0.0248	0.0151	0.203	0.0288	0.0245	0.224	0.0327	0.0294	0.492	0.0347	0.0309

obtained coefficients of variation c_v indicate that a homogeneous illumination of the desired region is possible at least for $\alpha < 0.1$, demonstrating the feasibility of the proposed approach. The robustness of the algorithm with respect to geometry is illustrated by the fact that the achieved variations do not depend very much on the curvature.

It can also be observed how the penalty parameter α determines the tradeoff between the number of active optodes and the homogeneity of the illumination in the region of interest: larger values of α yield fewer optodes but less homogeneous illumination. This applies to all the models, independent of their curvature. The qualitative behavior of the computed sources for each

Table 4.3: Results for three-dimensional model. N indicates the number of active nodes, c_v the coefficient of variation obtained for the photon density in the observation domain for all the different values of α.

α	1.8	1.6	1.4	1.2	1.0	0.8	0.6	0.4	0.2
N	0	12	150	250	333	409	498	637	884
c_v	—	1.85	0.564	0.359	0.265	0.204	0.156	0.113	0.0672

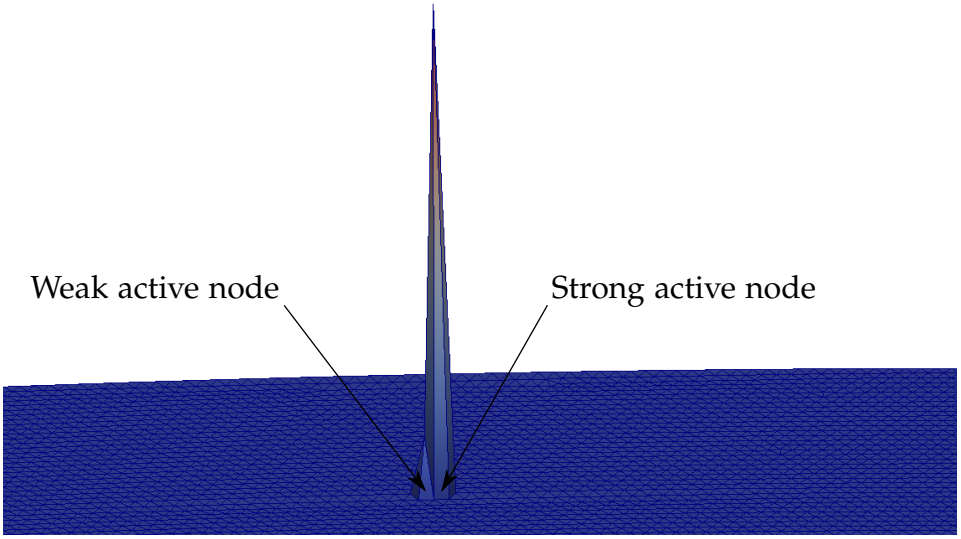

Figure 4.3: Detailed view showing a neighboring set of two active nodes appearing as one single optode in Figure 4.4. Single-curved model ($\kappa = 20$, $\alpha = 0.1$).

value of α is shown in Figure 4.4(a) and Figure 4.4(b) for a representative single-curved ($\kappa = 20$) and a double-curved model ($\kappa = 15$), respectively. The relative strength of the sources is coded by height. When comparing Tables 4.1 and 4.2 with Figure 4.4, it is obvious that fewer than the stated 15 optode positions are visible in Figure 4.4. This is due to the fact that quite often a weak active node is placed nearby a strong one (see Figure 4.3). These neighboring active nodes appear as a single peak and thus can be taken as a single optode.

While for the single-curved model and $\alpha = 0.1$ the distribution of optodes agrees well with the intuitive choice of equally spaced optodes of approximately equal magnitude, the other values indicate that a better illumination can be achieved with stronger sources towards the tips of the model. It should be pointed out that even in the former case, the number of optodes to be distributed is not obvious. For the double-curved models, the results indicate that optodes should be placed preferentially in regions where the curvature changes.

For reference, Figure 4.5 shows the corresponding photon densities φ_γ (in Wm^{-2}, normalized to unit mean) plotted along a part of the observation

region (for the left line in Figure 4.1). This illustrates how the parameter α and the model geometry influence the homogeneity of the illumination in this region. As expected, photon fluence shows the most pronounced inhomogeneities close to the borders. In the case of the single curved model, a nearly sinusoidal ripple pattern arises in more than 80 % of the target region, while in the double curved model the ripple is superimposed on a step-profile with the steps located approximately at the zero-crossing points of the curvature. With $\alpha = 0.1$, the peak–peak fluctuations are still around 40 % of the mean value even far away from the borders, which may be considered as unsatisfactory. However, when decreasing α to 0.01 or less, the ripple remains within a few percent, which is sufficient, especially when comparing this value to other sources of fluctuations of the irradiation such as local absorption changes by tissue inhomogeneities, bleeding, or inhomogeneities of the distribution of the photosensitizer.

The quantitative results for the three-dimensional model are shown in Table 4.3. For $\alpha = 1.8$, no controls are placed and thus the photon density is zero. This is consistent with the theory, which predicts that there is a threshold value for α above which the optimal control is identically zero (Casas, Clason, and Kunisch, 2012).

Figure 4.6 shows location and magnitude (color coded) of the computed optodes and the corresponding photon densities (in Wm^{-2}, normalized to unit mean) for $\alpha = 1.2$, $\alpha = 0.8$, and $\alpha = 0.4$. Due to the nonuniform curvature of the model, a homogeneous illumination is harder to achieve than in the two-dimensional case, especially at the borders of the target region. However, for $\alpha < 1.2$, the inhomogeneities in the interior are usually within 10 %, and the few hot spots of 30 % would probably still be acceptable because usually the pads are wrapped by additional stray layers (very strong scattering blood and fluids). Although of course the specific placement may be difficult to realize in practice, the qualitative distribution can be a very useful information during the initial design process.

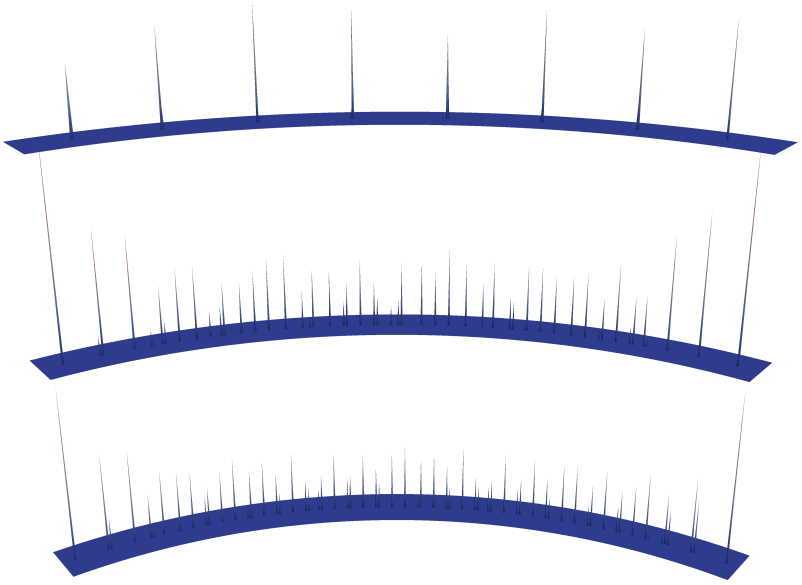

(a) Single-curved model ($\kappa = 20$).

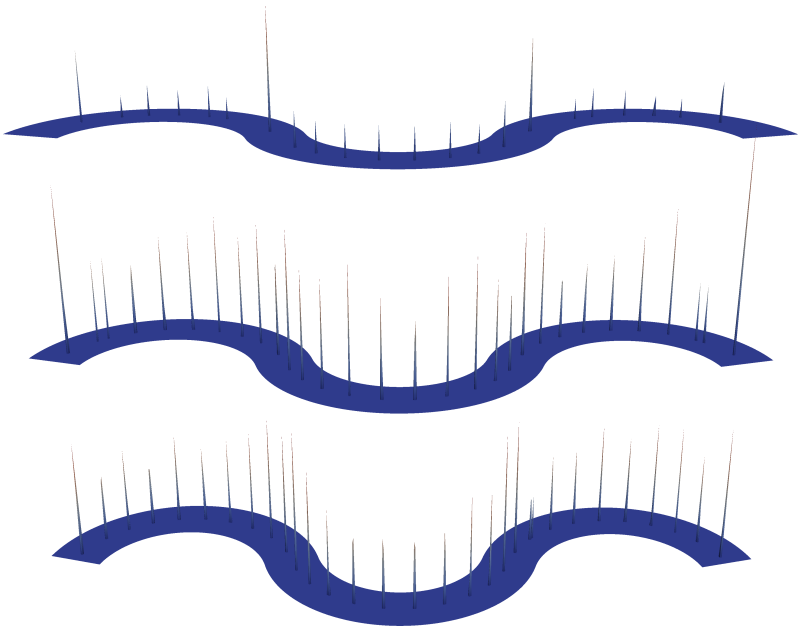

(b) Double-curved model ($\kappa = 15$).

Figure 4.4: Optode positions and relative magnitudes (height-coded) for representative single-curved and double-curved models for three different values of alpha (from top to bottom: $\alpha = 0.1$, $\alpha = 0.01$, $\alpha = 0.001$). From Brunner et al., 2012.

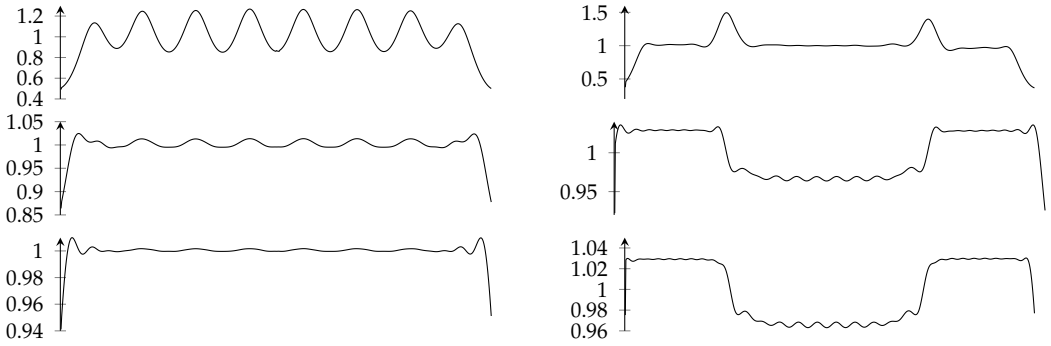

(a) Single-curved model ($\kappa = 20$). (b) Double-curved model ($\kappa = 15$).

Figure 4.5: Photon densities φ_γ (in Wm^{-2}, normalized to unit mean) plotted along part of the observation region (left line in Fig. 4.1) for representative single-curved and double-curved models for three different values of alpha (from top to bottom: $\alpha = 0.1$, $\alpha = 0.01$, $\alpha = 0.001$). From Brunner et al., 2012.

4.5 Discussion

The proposed approach is able to generate reasonable optode configurations adapted to specific geometries, even in situations where optimal setups are not intuitively obvious (such as in complex three-dimensional models). Our method also yields relative strengths of the optodes to be placed, which would otherwise have to be computed in a separate step. Furthermore, the algorithm is deterministic and does not require a-priori knowledge such as an initial set of candidate locations or the number of optodes required, which on the contrary is provided by our approach. The method can be used as a tool during the initial design process to estimate the number of sources required as well as their location and relative strengths.

By formulating the optode placement problem as a continuous optimization problem, the combinatorial complexity inherent in discrete approaches is avoided. This is critical for achieving an efficient optimization technique and has not been presented before in the context of diffuse optical imaging. As an example, our Python implementation required about three minutes on a MacBook Pro (2.16 GHz Intel Core2 Duo with 2 GByte RAM) for the single-curved model with $\kappa = 5$. Our approach could therefore also be used

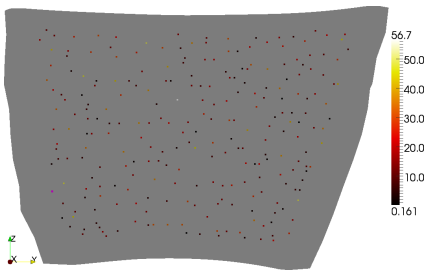

(a) Optodes, $\alpha = 1.2$.

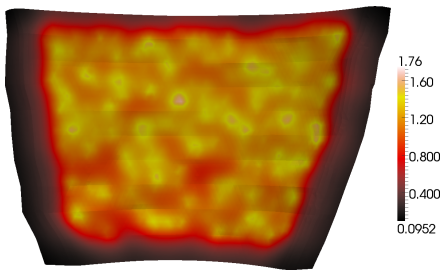

(b) Photon density, $\alpha = 1.2$.

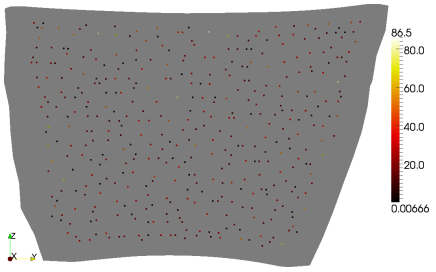

(c) Optodes, $\alpha = 0.8$.

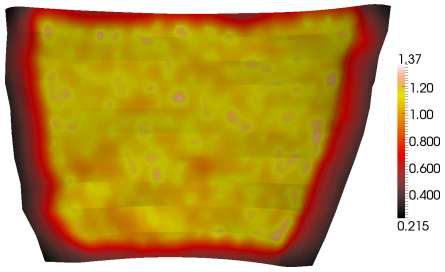

(d) Photon density, $\alpha = 0.8$.

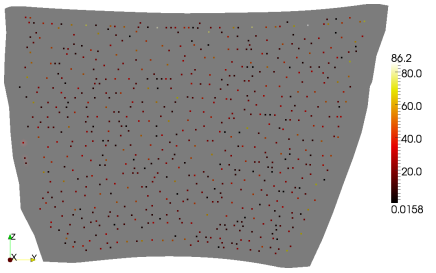

(e) Optodes, $\alpha = 0.4$.

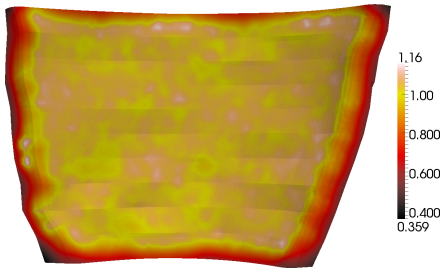

(f) Photon density, $\alpha = 0.4$.

Figure 4.6: Optode positions and magnitudes (left) and photon densities (right) (in Wm^{-2}, normalized to unit mean) for the three-dimensional model and three different values of α. From Brunner et al., 2012.

in an interactive setting, where the engineer will adapt design parameters, such as the optical coefficients of the diffuser, based on the outcome of an optimization run.

While the number of desired optodes is correlated with the penalty parameter α, it is not directly controllable. This drawback is analogous to the problem of finding the "best" regularization parameter in image reconstruction (e. g. for DOT), where typically the determination of the parameter is left to the user or is based on heuristics. Certainly, one could think about finding a good parameter through successive optimization runs, for example with decreasing values of α if the user specified the maximum number of optodes.

The achieved results are satisfactory from a mathematical point of view; but of course they should also be discussed in an engineering context. In particular, it may be difficult to place many sources in a more or less irregular pattern. The number of optodes depends on the required uniformity of the surface fluence. A reasonable value in practice would be a CV of 0.05. Table 4.1 shows CVs (for single-curved pads) below 0.03 for around 50 optodes, but up to 0.25 for less than 25 optodes. The numbers for the double-curved pad are only slightly greater. This means that a value of 40 to 50 required sources can be expected. In practice, such a design can be approximated relatively easily with parallel arranged cylindrical polymer diffusers of sufficiently small radii, which are fed by individual optical fibers. Instead of a fixed grid of diffusers, one can imagine dense bundles of uniformly spaced diffusers where only those close to the optimal positions are connected to the laser source. This would allow a very flexible use and adaptive homogenization of the fluence dependent on the individual anatomical situation (like, for example, different curvatures), which is certainly desirable in the context of a personalized optimization. Such a concept can be realized by using fiberoptic switches with many channels. In three dimensions, the sources may be fiber-coupled spherical diffusers or simply open-ended fibers. Due to the higher number of potential positions (637 for a CV of 0.11, see Table 4.3), the construction of a flexible structure may be difficult here, and pre-fabricated pads that are adapted to a certain anatomical target geometry appear more realistic than a truly adaptive system.

Although a rigorous sensitivity analysis has not yet been carried out, our experience indicates that the computed photon density distributions are relatively robust to small perturbations of the optode locations and magnitudes. Similarly, we did not observe significant changes in the results due to small random perturbations of the optical parameters. This can be attributed to the linearity and the strong diffusivity of the model (4.1). Such robustness is very important for practical implementations because it means that the result is not sensitive to manufacturing tolerances.

One of the main advantages of the optimal control approach is its flexibility. For example, it is straightforward to extend the underlying model to include inhomogeneous material properties or to replace the diffusion approximation by a more complicated model such as the radiative transfer equation. It is also possible to consider different objective criteria such as the photon flux through a given (boundary or internal) surface by changing the functional $J(q)$.

In principle, the approach can be applied to the problem of optimal experiment design for optical tomography if the objective $J(q)$ is based on a suitable sensitivity term. However, this extension of our method is subject to future work.

5 Conclusion

The aim of this work was to show the use of design optimization for improving soft field applications (SFAs) so they might become an important clinical tool. We demonstrate this using two specific examples.

The first tackled problem is an enhanced sensor and modeling system for BIA, which estimates the composition of body fat (BF) and fat free mass (FFM) inside the body.

Usually, simple cylinder models, which relate the measured impedance to the geometry of the human body, are used (see e. g. Kyle et al., 2004a). Here, measurement and injection electrodes are placed on hand/foot and wrist/ankle, respectively. Importantly, these models suffer from low sensitivities (Baumgartner, Ross, and Heymsfield, 1998).

In this work, a realistic three-dimensional model of the human thorax (truncated about 8 cm above and below the umbilicus) was developed. The electrode placement was chosen in a way that the penetrating electric current can pass the region of interest, namely the abdominal region. All parameters of interest, like the fat fraction in the muscle compartment, the visceral fat fraction, and the thickness of the subcutaneous fat layer, were directly incorporated using a hierarchical model. This model maps these properties to the conductivities of the different compartments (subcutaneous fat layer, abdominal muscle, mesenteric compartment, spine and bone). Such a structural model facilitates the detailed analysis of body composition measurements using BIA. The sensitivity analysis can be used to analyze important questions regarding the design of BIA systems such as which parameters of interest incorporated in the abdominal model can be measured using the suggested setup. A detailed analysis of the obtained sensitivity values revealed a high sensitivity to the SFL and the fat content of the mesentery. The usual drawback of BIA is the dependence of the results on

the hydration state of the tissue. This problem still remains, and the analysis predicts a high sensitivity to the muscular extracellular volume (represented by the conductivity at low frequencies of the muscular compartment in the model). Therefore, comparable hydration states are a prerequisite for a reliable BIA analysis.

Although the proposed method provides a valuable tool for the assessment of BIA methods, some questions still remain unanswered. For example, the influence of changes in the model geometry, as well as the effect of models which show different values for the SFL on the partitioning of the overall sensitivity are not clarified yet. An extension of the model setup to a multi-electrode and multi-frequency measurement system including a fitting algorithm for the reconstruction of the parameters would be desirable in this context.

The second design optimization problem shows the applicability of a novel method for the deterministic optimization of sensor positions (Clason and Kunisch, 2011) for the specific application of PDT of intrathoracic cancer.

This therapy is a challenge, because the geometry of the intrathoracic cavity is very complex. Thus, the optimization of cylindrical diffusers (their positions as well as their individual magnitude), integrated in a bag of intralipid, is not trivial. To show the applicability of the method mentioned above, we developed simple two-dimensional FE models as well as a realistic three-dimensional FE model of the human intrathoracic cavity. The homogeneity of the irradiation was assessed using the coefficient of variation of the photon density in the observation domain. Acceptable results would yield values equal to or below 0.05.

The results show that our method produces reasonable optode configurations for all models. A drawback might be the fact that the number of desired optodes cannot be set directly, but it is correlated with the penalty parameter α. However, using successive optimization runs with decreasing values of α until an upper level for the desired optodes is reached would be a straightforward solution. Obviously, the more homogeneous the surface fluence should be, the more optodes are necessary. For the two-dimensional models in this work, around 40 to 50 optodes were required to obtain a CV below 0.05. Although this number sounds rather high, such an applicator can be produced relatively easily using parallelly arranged cylindrical

polymer diffusers with a small radius, fed by optical fibers. The optimal optode positions could be found individually for every single patient. Using fiberoptic switches with many channels and a dense bundle of uniformly spaced diffusers connected to the laser source, only those optimal optode positions could be used. For the three-dimensional model, a number of 637 optodes would be needed to yield a CV of 0.11. Here, pre-fabricated pads are a solution, as individually adaptive systems would be quite difficult to implement.

The greatest advantages of using this optimization procedure for PDT is its efficiency (the locations and magnitudes of the optode positions are found in one single step and exponential complexity is avoided). In addition, it does not require an initial configuration. In this work, the underlying objective was the minimization of the photon density over the outer surface of the FE pads. Using other objectives is straightforward and thus the proposed procedure can be extended to a wide variety of problems of design optimization for OT.

Bibliography

Adler, A., Amato, M. B., Arnold, J. H., Bayford, R., Bodenstein, M., Böhm, S. H., Brown, B. H., Frerichs, I., Stenqvist, O., Weiler, N., and Wolf, G. K. (2012). "Whither lung EIT: where are we, where do we want to go and what do we need to get there?" In: *Physiological Measurement* 33.5, p. 679. DOI: 10.1088/0967-3334/33/5/679 (cit. on p. 2).

Agostinis, P., Berg, K., Cengel, K. A., Foster, T. H., Girotti, A. W., Gollnick, S. O., Hahn, S. M., Hamblin, M. R., Juzeniene, A., Kessel, D., Korbelik, M., Moan, J., Mroz, P., Nowis, D., Piette, J., Wilson, B. C., and Golab, J. (2011). "Photodynamic therapy of cancer: an update." In: *CA: A Cancer Journal for Clinicians* 61.4, pp. 250–281. ISSN: 1542-4863. DOI: 10.3322/caac.20114 (cit. on p. 18).

Allison, R. R. and Sibata, C. H. (2010). "Oncologic photodynamic therapy photosensitizers: a clinical review." In: *Photodiagnosis and photodynamic therapy* 7.2, pp. 61–75 (cit. on p. 20).

Ampère, A.-M. (1827). "Mémoire sur la théorie mathématique des phénomènes électro-dynamiques uniquement déduite de l'expérience." In: *Mémoires de l'Académie royale des Sciences de l'Institut de Frances*, pp. 175–388 (cit. on p. 6).

Arridge, S. R. (1999). "Optical tomography in medical imaging." In: *Inverse problems* 15.2, R41 (cit. on pp. 1, 10, 26, 52).

Baas, P., Murrer, L., Zoetmulder, F. A., Stewart, F. A., Ris, H. B., van Zandwijk, N., Peterse, J. L., and Rutgers, E. J. (1997). "Photodynamic therapy as adjuvant therapy in surgically treated pleural malignancies." In: *Br. J. Cancer* 76.6, pp. 819–826 (cit. on p. 50).

Babilas, P. and Szeimies, R. M. (2010). "The use of photodynamic therapy in dermatology." In: *Giornale italiano di dermatologia e venereologia: organo ufficiale, Societa Italiana di Dermatologia e Sifilografia* 145.5, pp. 613–630 (cit. on p. 50).

Baumgartner, R. N., Chumela, W. C., and Roche, A. F. (1989). "Estimation of body composition from bioelectric impedance of body segments." In: *American Journal of Clinical Nutrition* 50, pp. 221–226 (cit. on p. 29).

Baumgartner, R. N., Ross, R., and Heymsfield, S. B. (1998). "Does adipose tissue influence bioelectric impedance in obese men and women?" In: *Journal of Applied Physiology* 84.1, pp. 257–262 (cit. on pp. 4, 29, 30, 68).

Bayford, R. H. (2006). "Bioimpedance tomography (electrical impedance tomography)." In: *Annu. Rev. Biomed. Eng.* 8, pp. 63–91 (cit. on p. 1).

Beer, A. (1852). "Bestimmung der Absorption des rothen Lichts in farbigen Flüssigkeiten." In: *Annalen der Physik und Chemie* 86, pp. 78–88 (cit. on p. 9).

Bhurosy, T. and Jeewon, R. (2014). "Overweight and obesity epidemic in developing countries: a problem with diet, physical activity, or socioeconomic status?" In: *The Scientific World Journal* 2014. DOI: http://dx.doi.org/10.1155/2014/964236 (cit. on p. 29).

Boltzmann, L. (1970). "Weitere Studien über das Wärmegleichgewicht unter Gasmolekülen." In: *Kinetische Theorie II*. Vol. 67. WTB Wissenschaftliche Taschenbücher. Vieweg+Teubner Verlag, pp. 115–225. ISBN: 978-3-528-06067-1. DOI: 10.1007/978-3-322-84986-1_3 (cit. on p. 10).

Bouguer, P. (1729). *Essai d'optique sur la gradation de la lumière*. Paris: C. Jombert (cit. on p. 9).

Bozler, E. and Cole, K. S. (1935). "Electric impedance and phase angle of muscle in rigor." In: *Journal of Cellular and Comparative Physiology* 6.2, pp. 229–241 (cit. on p. 11).

Brancaleon, L. and Moseley, H. (2002). "Laser and non-laser light sources for photodynamic therapy." In: *Lasers in Medical Science* 17.3, pp. 173–186 (cit. on p. 20).

Bright, R. (1831). "Diseases of the brain and nervous system." In: *London, UK: Longman* 2, p. 431 (cit. on p. 11).

Brunner, P., Clason, C., Freiberger, M., and Scharfetter, H. (2012). "A deterministic approach to the adapted optode placement for illumination of highly scattering tissue." In: *Biomedical Optics Express* 3.7, pp. 1732–1743 (cit. on pp. 4, 57, 59, 63–65).

Calderón, A. P. (2006). "On an inverse boundary problem." In: *Mat. Apl. Comput.* 25 (2–3), pp. 133–138 (cit. on p. 2).

Casas, E., Clason, C., and Kunisch, K. (2012). "Approximation of elliptic control problems in measure spaces with sparse solutions." In: *SIAM*

Journal on Control and Optimization 50.4, pp. 1735–1752 (cit. on pp. 55, 62).

Chandrasekhar, S. (1950). *Radiative transfer*. Vol. 1. Oxford, Clarendon Press, 1950. (cit. on p. 10).

Chatziioannidis, I., Samaras, T., Mitsiakos, G., Karagianni, P., and Nikolaidis, N. (2013). "Assessment of lung ventilation in infants with respiratory distress syndrome using electrical impedance tomography." In: *Hippokratia* 17.2, pp. 115–119 (cit. on p. 3).

Cheney, M., Isaacson, D., and Isaacson, E. L. (1990). "Exact solutions to a linearized inverse boundary value problem." In: *Inverse Problems* 6, pp. 923–934 (cit. on p. 37).

Cheney, M., Isaacson, D., and Newell, J. C. (1999). "Electrical Impedance Tomography." In: *SIAM Review* 41.1, pp. 85–101. ISSN: 00361445 (cit. on p. 24).

Chwolson, O. (1889). "Grundzüge einer mathematischen Theorie der inneren Diffusion des Lichtes." In: *Bull. Acad. Imp. Sci., St. Petersbourg* 33, pp. 221–256 (cit. on p. 9).

Clason, C. and Kunisch, K. (2011). "A duality-based approach to elliptic control problems in non-reflexive Banach spaces." In: *ESAIM Contr. Optim. Ca.* 17.1, pp. 243–266. DOI: 10.1051/cocv/2010003 (cit. on pp. 53, 69).

Clason, C. and Kunisch, K. (2012). "A measure space approach to optimal source placement." In: *Computational Optimization and Applications* 53.1, pp. 155–171 (cit. on pp. 54, 56).

Cole, K. S. (1928). "Electric impedance of suspensions of spheres." In: *The Journal of General Physiology* 12.1, pp. 29–36 (cit. on p. 11).

Cole, K. S. (1940). "Permeability and Impermeability of Cell Membranes for Ions." In: *Cold Spring Harb Symp Quant Biol* 8, pp. 110–122. DOI: 10.1101/SQB.1940.008.01.013 (cit. on p. 14).

Cole, K. S. and Curtis, H. J. (1938). "Electric impedance of Nitella during activity." In: *The Journal of General Physiology* 22.1, pp. 37–64 (cit. on p. 11).

Cole, K. S. and Curtis, H. J. (1939). "Electric impedance of the squid giant axon during activity." In: *The Journal of General Physiology* 22.5, pp. 649–670 (cit. on p. 11).

Cox, B. (2014). *Introduction to Tissue Optics*. URL: http://www.ucl.ac.uk/medphys/staff/people/bcox/BenCox_TissueOptics.pdf (cit. on p. 26).

Culver, J. P., Ntziachristos, V., Holboke, M. J., and Yodh, A. G. (2001). "Optimization of optode arrangements for diffuse optical tomography: a singular-value analysis." In: *Opt. Lett.* 26, pp. 701–703 (cit. on p. 49).

Curtis, H. J. and Cole, K. S. (1938). "Transverse electric impedance of the squid giant axon." In: *The Journal of General Physiology* 21.6, pp. 757–765 (cit. on p. 11).

Cutler, M. (1931a). "Transillumination as an Aid in the Diagnosis of Breast Lesions." In: *Surg. Gynec. and Obst.* 48, p. 721 (cit. on p. 12).

Cutler, M. (1931b). "Transillumination of the breast." In: *Annals of Surgery* 93.1, pp. 223–234. ISSN: 0003-4932 (cit. on p. 12).

DeFronzo, R. A., Bergenstal, R. M., Bode, B., Kushner, R., Lewin, A. J., Skjøth, T. V., Jensen, C. B., and Davies, M. (2014). "Effects of Liraglutide 3.0 Mg and 1.8 Mg on Body Weight and Cardiometabolic Risk Factors in Overweight and Obese Adults with Type 2 Diabetes Mellitus (T2DM): The Scale Diabetes Randomized, Double-Blind, Placebo-Controlled, 56-Week Trial." In: (cit. on p. 29).

Dhatt, G., Lefrançois, E., and Touzot, G. (2012). *Finite Element Method*. John Wiley & Sons. ISBN: 9781118569702 (cit. on p. 28).

Dolmans, D. E., Fukumura, D., and Jain, R. K. (2003). "Photodynamic therapy for cancer." In: *Nat. Rev. Cancer* 3.5, pp. 380–387 (cit. on p. 50).

Duck, F. A. (2013). *Physical properties of tissues: a comprehensive reference book*. Academic Press (cit. on p. 12).

Dwyer, P. J., White, W. M., Fabian, R. L., and Anderson, R. R. (2000). "Optical integrating balloon device for photodynamic therapy." In: *Lasers Surg. Med.* 26.1, pp. 58–66 (cit. on p. 50).

E. Haber, U. M. Ascher and Oldenburg, D. (2000). "On optimization techniques for solving nonlinear inverse problems." In: *Inverse Problems* 16, pp. 1263–1280 (cit. on p. 3).

Elia, M. and Ward, L. C. (1999). "New techniques in nutritional assessment: body composition methods." In: *Proceedings of the Nutrition Society* 58, pp. 33–38 (cit. on p. 47).

Ferrari, M. and Quaresima, V. (2012). "A brief review on the history of human functional near-infrared spectroscopy (fNIRS) development and fields of application." In: *NeuroImage* 63.2, pp. 921–935. ISSN: 1053-8119. DOI: 10.1016/j.neuroimage.2012.03.049 (cit. on p. 1).

Foster, K. R. and Schwan, H. P. (1995). "Dielectric properties of tissues." In: *Handbook of biological effects of electromagnetic fields* 2, pp. 25–102 (cit. on p. 13).

Freiberger, M., Clason, C., and Scharfetter, H. (2010). "Total Variation Regularization for Nonlinear Fluorescence Tomography with an Augmented Lagrangian Splitting Approach." In: *Appl. Optics* 49.19, pp. 3741–3747. DOI: 10.1364/AO.49.003741 (cit. on p. 53).

Fricke, H. (1924). "A Mathematical Treatment of the Electric Conductivity and Capacity of Disperse Systems I. The Electric Conductivity of a Suspension of Homogeneous Spheroids." In: *Phys. Rev.* 24 (5), pp. 575–587. DOI: 10.1103/PhysRev.24.575 (cit. on pp. 40, 42).

Fricke, H. and Morse, S. (1925). "The electric resistance and capacity of blood for frequencies between 800 and 41/2 million cycles." In: *The Journal of General Physiology* 9.2, p. 153 (cit. on p. 11).

Friedberg, J. S., Mick, R., Stevenson, J., Metz, J., Zhu, T., Buyske, J., Sterman, D. H., Pass, H. I., Glatstein, E., and Hahn, S. M. (2003). "A phase I study of Foscan-mediated photodynamic therapy and surgery in patients with mesothelioma." In: *Ann. Thorac. Surg.* 75.3, pp. 952–959 (cit. on pp. 50, 51).

Gabriel, C., Gabriel, S., and Corthout, E. (1996). "The dielectric properties of biological tissues: 1. Literature survey." In: *Physics in Medicine and Biology* 41, pp. 2231–2249 (cit. on p. 39).

Gabriel, S., Lau, R. W., and Corthout, E. (1996). "The dielectric properties of biological tissues: 2. Measurements in the frequency range 10 Hz to 20 GHz." In: *Physics in Medicine and Biology* 41, pp. 2251–2269 (cit. on p. 39).

Gabriel, S., Lau, R. W., and Gabriel, C. (1996). "The dielectric properties of biological tissues: 3. Parametric models for the dielectric spectrum of tissues." In: *Physics in Medicine and Biology* 41, pp. 2271–2293 (cit. on p. 39).

Gans, R. (1924). "Die Farbe des Meeres." In: *Annalen der Physik* 380.17, pp. 1–22. ISSN: 1521-3889. DOI: 10.1002/andp.19243801702 (cit. on p. 10).

Gauss, C. F. (1867). *Werke*. Vol. 5, p. 602 (cit. on p. 6).

Geddes, L. A. and Baker, L. E. (1967). "The specific resistance of biological material – a compendium of data for the biomedical engineer and physiologist." In: *Medical and Biological Engineering* 5, pp. 271–293 (cit. on pp. 39, 42).

Gibson, A. and Dehghani, H. (2009). "Diffuse optical imaging." In: *Philosophical Transactions of the Royal Society of London A: Mathematical, Physical and Engineering Sciences* 367.1900, pp. 3055–3072 (cit. on p. 12).

Gielen, F. L. H., Jonge, W. Wallinga-de, and Boon, K. L. (1984). "Electrical conductivity of skeletal muscle tissue: experimental results from different muscles in vivo." In: *Medical and Biological Engineering and Computing* 22, pp. 569–577 (cit. on p. 39).

Gonzalez, C. A., Zuniga, O., and Padilla, L. E. (1997). "Detection of animal tissue thickness using simple vertical electric sounding (VES)." In: *Physiological Measurements* 18, pp. 85–91 (cit. on p. 33).

Gratton, G., Corballis, P. M., Cho, E., Fabiani, M., and Hood, D. C. (1995). "Shades of gray matter: Noninvasive optical images of human brain reponses during visual stimulation." In: *Psychophysiology* 32.5, pp. 505–509 (cit. on p. 12).

Graves, E. E., Culver, J. P., Ripoll, J., Weissleder, R., and Ntziachristos, V. (2004). "Singular-value analysis and optimization of experimental parameters in fluorescence molecular tomography." In: *J. Opt. Soc. Am. A* 21, pp. 231–241 (cit. on p. 49).

Griffiths, H. (2001). "Magnetic induction tomography." In: *Measurement Science and Technology* 12.8, p. 1126 (cit. on p. 1).

Hanai, T. (1960). "Theory of the dielectric dispersion due to the interfacial polarization and its application to emulsions." In: *Colloid Journal* 171, pp. 23–31 (cit. on p. 42).

Hassan, A. M. and El-Shenawee, M. (2011). "Review of electromagnetic techniques for breast cancer detection." In: *IEEE Reviews in Biomedical Engineering* 4, pp. 103–118 (cit. on p. 2).

Heaviside, O. (1894). *Electrical Papers*. Vol. 2. MacMillan (cit. on p. 7).

Henderson, B. W., Busch, T. M., Vaughan, L. A., Frawley, N. P., Babich, D., Sosa, T. A., Zollo, J. D., Dee, A. S., Cooper, M. T., Bellnier, D. A., Greco, W. R., and Oseroff, A. R. (2000). "Photofrin Photodynamic Therapy Can Significantly Deplete or Preserve Oxygenation in Human Basal Cell Carcinomas during Treatment, Depending on Fluence Rate." In: *Canc. Treat.* 60, pp. 525–529 (cit. on p. 52).

Hermann, L. (1870). "Weitere Untersuchungen über die Ursache der electromotorischen Erscheinungen an Muskeln und Nerven." In: *Archiv für die gesamte Physiologie des Menschen und der Tiere* 3.1, pp. 15–39. ISSN: 0365-267x. DOI: 10.1007/BF01855744 (cit. on p. 10).

Hertz, H. R. (1892). *Untersuchungen über die Ausbreitung der elektrischen Kraft*. Leibzig (cit. on p. 7).

Hofvind, S., Ponti, A., Patnick, J., Ascunce, N., Njor, S., Broeders, M., Giordano, L., Frigerio, A., and Törnberg, S. (2012). "False-positive results in mammographic screening for breast cancer in Europe: a literature review and survey of service screening programmes." In: *J Med Screen* 19 (suppl 1), pp. 57–66. ISSN: 0969-1413, 1475-5793. DOI: 10.1258/jms.2012.012083 (cit. on p. 2).

Houtkooper, L. B., Lohman, T. G., Going, S. B., and Howell, W. H. (1996). "Why bioelectrical impedance analysis should be used for estimating adiposity." In: *The American journal of clinical nutrition* 64.3, 436S–448S (cit. on p. 3).

Hu, Y., Wang, K., and Zhu, T. C. (2009). "A light blanket for intraoperative photodynamic therapy." In: *Proceedings of SPIE* 7380. Ed. by D. H. Kessel, 73801W. DOI: 10.1117/12.823064 (cit. on p. 51).

Hu, Y., Wang, K., and Zhu, T. C. (2010). "Pre-clinic study of uniformity of light blanket for intraoperative photodynamic therapy." In: *Proceedings of SPIE* 7551. Ed. by D. H. Kessel, p. 755112. DOI: 10.1117/12.842809 (cit. on p. 51).

Huang, Z., McWilliams, A., Lui, H., McLean, D. I., Lam, S., and Zeng, H. (2003). "Near-infrared Raman spectroscopy for optical diagnosis of lung cancer." In: *International Journal of Cancer* 107.6, pp. 1047–1052. ISSN: 1097-0215. DOI: 10.1002/ijc.11500 (cit. on p. 3).

Huray, P. G. (2010). "Foundations of Maxwell's Equations." In: *Maxwell's Equations*. John Wiley and Sons, Inc. ISBN: 9780470549919 (cit. on p. 21).

Huynh, P. T., Jarolimek, A. M., and Daye, S. (1998). "The false-negative mammogram." In: *RadioGraphics* 18.5, pp. 1137–1154. ISSN: 271-5333. DOI: 10.1148/radiographics.18.5.9747612 (cit. on p. 2).

Jackson, W. H. (1910). "The solution of an integral equation occurring in the theory of radiation." In: *Bull. Amer. Math. Soc.* 16.9, pp. 473–475. URL: http://projecteuclid.org/euclid.bams/1183420786 (cit. on p. 10).

Jacobs, D. A. H. (1980). "Preconditioned conjugate gradient methods for solving systems of algebraic equations." In: *Central Electricity Lab* Lab Note 199/80 (cit. on p. 37).

Jacques, S. L. (2013). "Optical properties of biological tissues: a review." In: *Physics in medicine and biology* 58.11, R37 (cit. on p. 15).

Jöbsis, F. F. (1977). "Noninvasive, infrared monitoring of cerebral and myocardial oxygen sufficiency and circulatory parameters." In: 198.4323, pp. 1264–1267. ISSN: 0036-8075, 1095-9203. DOI: 10.1126/science.929199 (cit. on p. 12).

Johnston, S. F. (2001). *A History of Light and Colour Measurement. Science in the Shadows.* Bristol and Philadelphia: Institute of Physics Publishing (cit. on pp. 8, 9).

Jossinet, J. (1996). "Variability of impedivity in normal and pathological breast tissue." In: *Medical and Biological Engineering and Computing* 34, pp. 356–350 (cit. on p. 39).

Jossinet, J. (1998). "The impedivity of freshly excised human breast tissue." In: *Physiological Measurements* 19, pp. 61–75 (cit. on p. 39).

Juzeniene, A., Juzenas, P., Ma, L.-W., Iani, V., and Moan, J. (2004). "Effectiveness of different light sources for 5-aminolevulinic acid photodynamic therapy." In: *Lasers in medical science* 19.3, pp. 139–149 (cit. on p. 20).

Keller, J. B. (1976). "Inverse Problems." In: *American Mathem. Monthly* 83, pp. 107–118 (cit. on p. 1).

Kepler, J. (1604). *Ad Vitellionem paralipomena, quibus astronomiae pars optica traditur*. C. Mare und E. J. Aubry. URL: https://books.google.at/books?id=hFgeygAACAAJ (cit. on p. 9).

Kershaw, D. S. (1978). "The incomplete Cholesky-conjugate gradient method for iterative solution of systems of linear equations." In: *Journal of Computational Physics* 26, pp. 43–65 (cit. on p. 37).

King, L. V. (1913). "On the Scattering and Absorption of Light in Gaseous Media, with Applications to the Intensity of Sky Radiation." In: *Proceedings of the Royal Society of London A: Mathematical, Physical and Engineering Sciences* 88.601, pp. 83–89. ISSN: 0950-1207. DOI: 10.1098/rspa.1913.0009 (cit. on p. 10).

Kondepati, V. R., Heise, M. H., and Backhaus, J. (2008). "Recent applications of near-infrared spectroscopy in cancer diagnosis and therapy." In: *Analytical and Bioanalytical Chemistry* 390.1, pp. 125–139. ISSN: 1618-2642. DOI: 10.1007/s00216-007-1651-y (cit. on p. 3).

Kotanko, P., Levin, N. W., and Zhu, F. (2008). "Current state of bioimpedance technologies in dialysis." In: *Nephrology Dialysis Transplantation* 23.3, pp. 808–812 (cit. on p. 3).

Krueger, T., Altermatt, H. J., Mettler, D., Scholl, B., Magnusson, L., and Ris, H.-B. (2003). "Experimental photodynamic therapy for malignant

pleural mesothelioma with pegylated mTHPC." In: *Lasers Surg. Med.* 32.1, pp. 61–68. DOI: 10.1002/lsm.10113 (cit. on p. 50).

Kyle, U. G., Bosaeus, I., De Lorenzo, A. D., Deurenberg, P., Elia, M., Gómez, J. M., Heitmann, B. L., Kent-Smith, L., Melchior, J.-C., Pirlich, M., Scharfetter, H., Schols, A. M. W. J., and Pichard, C. (2004a). "Bioelectrical impedance analysis – part I: review of principles and methods." In: *Clinical Nutrition* 23.5, pp. 1226–1243 (cit. on pp. 1, 11, 30, 68).

Kyle, U. G., Bosaeus, I., De Lorenzo, A. D., Deurenberg, P., Elia, M., Gómez, J. M., Heitmann, B. L., Kent-Smith, L., Melchior, J.-C., Pirlich, M., Scharfetter, H., Schols, A. M. W. J., and Pichard, C. (2004b). "Bioelectrical impedance analysis – part II: utilization in clinical practice." In: *Clinical Nutrition* 23.6, pp. 1430–1453 (cit. on p. 3).

Lambert, J. H. (1760). *Photometrica: Sive de Mensura de Gratibus Luminis, Colorum et Umbrae*. Augsburg: Eberhard Klett (cit. on p. 9).

Lambert, J. H. and DiLaura, D. L. (2001). *Photometry or On the Measure and Gradation of Light, Colors, and Shade*. Illuminating Engineering Society of North America (cit. on p. 9).

Lasser, T. and Ntziachristos, V. (2007). "Optimization of 360° projection fluorescence molecular tomography." In: *Med. Image Anal.* 11, pp. 389–399 (cit. on p. 50).

Lenz, H. F. E. (1834). "Ueber die Bestimmung der Richtung der durch elektrodynamische Vertheilung erregten galvanischen Ströme." In: *Annalen der Physik und Chemie* 107, pp. 483–494 (cit. on p. 7).

Lessig, C., Fiume, E., and Desbrun, M. (2012). "On the mathematical formulation of radiance." In: *arXiv:1205.4447 [math-ph, physics:physics]*. arXiv: 1205.4447. URL: http://arxiv.org/abs/1205.4447 (cit. on p. 10).

Lim, C.-K., Heo, J., Shin, S., Jeong, K., Seo, Y. H., Jang, W.-D., Park, C. R., Park, S. Y., Kim, S., and Kwon, I. C. (2013). "Nanophotosensitizers toward advanced photodynamic therapy of cancer." In: *Cancer Letters* 334.2, pp. 176–187 (cit. on p. 20).

Logg, A., Mardal, K.-A., and Wells, G. N. (2012). *Automated Solution of Differential Equations by the Finite Element Method*. Software available from http://fenicsproject.org. Springer. ISBN: 978-3-642-23098-1. DOI: 10.1007/978-3-642-23099-8 (cit. on p. 56).

Lommel, E. (1889). "Die Photometrie der diffusen Zurückwerfung." In: *Annalen der Physik* 272.2, pp. 473–502 (cit. on p. 9).

Lukaski, H. C. (1987). "Methods for the assessment of human body composition: traditional and new." In: *American Journal of Clinical Nutrition* 46, pp. 537–556 (cit. on p. 29).

Maxwell, J. C. (1865). "A dynamical theory of the electromagnetic field." In: *Philosophical Transactions of the Royal Society of London*, pp. 459–512 (cit. on p. 7).

McNeill, G., Fowler, P. A., Maughan, R. J., McGaw, B. A., Fuller, M. F., Gvozdanovic, D., and Gvozdanovic, S. (1991). "Body fat in lean and overweight woman estimated by six methods." In: *British Journal of Nutrition* 65, pp. 95–103 (cit. on p. 29).

McRae, D. A. and Esrick, M. A. (1993). "Changes in electrical impedance of skeletal muscle measured during hyperthermia." In: *International Journal of Hyperthermia* 9.2, pp. 247–261 (cit. on p. 39).

Mishchenko, M. I. (2008). "Multiple scattering, radiative transfer, and weak localization in discrete random media: unified microphysical approach." In: *Reviews of Geophysics* 46.2 (cit. on pp. 10, 25).

Mishchenko, M. I. (2013). "125 years of radiative transfer: enduring triumphs and persisting misconceptions." In: *AIP Conference Proceedings*. Vol. 1531. AIP Publishing, pp. 11–18. DOI: 10.1063/1.4804696 (cit. on pp. 9, 10).

Mukhopadhyay, S. C., Lay-Ekuakille, A., and Fuchs, A. (2011). *New Developments and Applications in Sensing Technology*. Springer Science & Business Media. ISBN: 978-3-642-17943-3 (cit. on p. 1).

Murthy, K. P. N. (2006). "Ludwig Boltzmann, Transport Equation and the Second law." In: *arXiv preprint cond-mat/0601566* (cit. on p. 10).

Nahin, P. J. (2002). *Oliver Heaviside: The Life, Work and Times of an Electrical Genius of the Victorian Age*. JHU Press (cit. on p. 7).

Neumann, F. (1845). *Die mathematischen Gesetze der induzierten elektrischen Ströme*, pp. 15–18 (cit. on p. 7).

Organ, L. W., Bradham, G. B., Gore, D. W., and Lozier, S. L. (1994). "Segmental bioelectrical impedance analysis: theory and application of a new technique." In: *Journal of Applied Physiology* 77, pp. 98–112 (cit. on p. 29).

Ørsted, H. C. (1830). "Thermo-electricity." In: *Edinburgh Encyclopaedia* XVIII, pp. 573–589 (cit. on p. 5).

Pethig, R. and Schmueser, I. (2012). "Marking 100 years since Rudolf Höber's discovery of the insulating envelope surrounding cells and of the beta-dispersion exhibited by tissue." In: DOI: 10.5617/jeb.401 (cit. on p. 11).

Philippson, M. (1920). "Sur la résistance électrique des cellules et des tissus." In: *Soc. Biol* 83, pp. 1399–1402 (cit. on pp. 11, 14).

Planck, M. (1914). *The theory of heat radiation*. Courier Corporation (cit. on p. 9).

Rigaud, B., Hamzaoui, L., Chauveau, N., Granié, M., Rinaldi, J. P. Scotto Di, and Morucci, J. P. (1994). "Tissue characterization by impedance: a multifrequency approach." In: *Physiological Measurements* 15, A13–A20 (cit. on pp. 40, 42).

Rigaud, B., Hamzaoui, L., Frikha, M. R., Chauveau, N., and Morucci, J. P. (1995). "In vitro tissue characterization and modelling using electrical impedance measurements in the 100 Hz–10 MHz frequency range." In: *Physiological Measurements* 16 (3 Suppl. A), A15–A28 (cit. on p. 40).

Robinson, E. S. and Coruh, C. (1988). "Geoelectrical surveying." In: *Basic Exploration in Geophysics* 13, pp. 445–500 (cit. on p. 47).

Rothmaier, M., Selm, B., Spichtig, S., Haensse, D., and Wolf, M. (2008). "Photonic textiles for pulse oximetry." In: *Opt. Express* 16.17, pp. 12973–12986 (cit. on p. 51).

Rush, S., Abildskov, J. A., and McFee, R. (1963). "Resistivity of body tissues at low frequencies." In: *Circulation Research* 12, pp. 40–50 (cit. on p. 39).

Scharfetter, H., Brunner, P., Mayer, M., Brandstätter, B., and Hinghofer-Szalkay, H. (2005). "Fat and hydration monitoring by abdominal bioimpedance analysis: data interpretation by hierarchical electrical modeling." In: *IEEE Transactions on Biomedical Engineering* 52.6, pp. 975–982 (cit. on pp. 4, 31, 32, 36, 38).

Scharfetter, H., Schlager, T., Stollberger, R., Felsberger, R., Hutten, H., and Hinghofer-Szalkay, H. (2001). "Assessing abdominal fatness with local bioimpedance analysis: basics and experimental findings." In: *International Journal of Obesity* 25, pp. 502–511 (cit. on pp. 30, 31, 33, 34, 37, 42, 44, 45, 47).

Schouwink, H. and Baas, P. (2004). "Foscan-mediated photodynamic therapy and operation for malignant pleural mesothelioma." In: *Ann. Thorac. Surg.* 78.1, p. 388. DOI: 10.1016/j.athoracsur.2003.08.088 (cit. on p. 50).

Schuster, A. (1905). "Radiation through a foggy atmosphere." In: *The Astrophysical Journal* 21, p. 1 (cit. on p. 9).

Schwan, H. P. (1957). "Electrical properties of tissue and cell suspensions." In: *Advances in biological and medical physics* 5, pp. 147–209 (cit. on pp. 11, 13).

Schwan, H. P. (1994). "Electrical properties of tissues and cell suspensions: mechanisms and models." In: DOI: 10.1109/IEMBS.1994.412155 (cit. on p. 11).

Scientific Biography, Complete Dictionary of (2015). *Hertz, H. R.* URL: http://www.encyclopedia.com/doc/1G2-2830901978.html (cit. on p. 8).

Segal, K. R., Loan, M. Van, Fitzgerald, P. I., Hodgon, J. A., and Itallie, T. B. Van (1988). "Lean body mass estimation by bioelectrical impedance analysis: a four-site cross-validation study." In: *American Journal of Clinical Nutrition* 47, pp. 7–14 (cit. on p. 29).

Selm, B., Rothmaier, M., Camenzind, M., Khan, T., and Walt, H. (2007). "Novel flexible light diffuser and irradiation properties for photodynamic therapy." In: *J. Biomed. Opt.* 12.3, p. 034024. DOI: 10.1117/1.2749737 (cit. on p. 51).

El-Shenawee, M. (2011). "Electromagnetic imaging for breast cancer research." In: pp. 55–58. DOI: 10.1109/BIOWIRELESS.2011.5724362 (cit. on p. 2).

Stadler, G. (2009). "Elliptic optimal control problems with L^1-control cost and applications for the placement of control devices." In: *Comput. Optim. Appl.* 44.2, pp. 159–181. DOI: 10.1007/s10589-007-9150-9 (cit. on p. 51).

The Royal Institution of Great Britain (2015). *Interactive timeline: Michael Faraday*. URL: http://www.ri.ac.uk/our-history/michael-faraday/about (cit. on p. 6).

Tuan, V.-D. (2003). *Biomedical Photonics Handbook*. CRC Press (cit. on p. 12).

van Veen, P., Schouwink, J. H., Star, W. M., Sterenborg, H. J., van der Sijp, J. R., Stewart, F. A., and Baas, P. (2001). "Wedge-shaped applicator for additional light delivery and dosimetry in the diaphragmal sinus during photodynamic therapy for malignant pleural mesothelioma." In: *Phys. Med. Biol.* 46.7, pp. 1873–1883 (cit. on p. 50).

Vorlesungen über die Theorie der Wärmestrahlung (1906). *Vorlesungen über die Theorie der Wärmestrahlung : Planck, Max, 1858–1947*. Leipzig. URL: https://archive.org/download/vorlesungenberd04plangoog/vorlesungenberd04plangoog.pdf (cit. on p. 9).

Wang, L., Jacques, S. L., and Zheng, L. (1995). "MCML – Monte Carlo modeling of light transport in multi-layered tissues." In: *Computer methods and programs in biomedicine* 47.2, pp. 131–146 (cit. on p. 28).

Wang, Y. and Lobstein, T. (2006). "Worldwide trends in childhood overweight and obesity." In: *International Journal of Pediatric Obesity* 1.1, pp. 11–25. DOI: 10.1080/17477160600586747 (cit. on p. 29).

Xiang, Y., Xu, K., Zhang, Z., Dai, Y., and Harrington, P. de B. (2010). "Near-infrared spectroscopic applications for diagnosis of endometrial carcinoma." In: *Journal of Biomedical Optics* 15.6, pp. 067002–067002 (cit. on p. 3).

Xu, H., Dehghani, H., Pogue, B. W., Springett, R., Paulsen, K. D., and Dunn, J. F. (2003). "Near-infrared imaging in the small animal brain: optimization of fiber positions." In: *J. Biomed. Opt.* 8.1, pp. 102–110. DOI: 10.1117/1.1528597 (cit. on p. 49).